REFERENCE RADIATION FOR COSMIC RAYS IN RBE RESEARCH

A Thesis

by

SHAOYONG FENG

Submitted to the Office of Graduate Studies of
Texas A&M University
in partial fulfillment of the requirements for the degree of

MASTER OF SCIENCE

August 2010

Major Subject: Health Physics

Reference Radiation for Cosmic Rays in RBE Research

REFERENCE RADIATION FOR COSMIC RAYS IN RBE RESEARCH

A Thesis

by

SHAOYONG FNEG

Submitted to the Office of Graduate Studies of
Texas A&M University
in partial fulfillment of the requirements for the degree of

MASTER OF SCIENCE

Approved by:

Chair of Committee,	Leslie A. Braby
Committee Members,	John R. Ford, Jr.
	Nancy D. Turner
Head of Department,	Raymond J. Juzaitis

August 2010

Major Subject: Health Physics

ABSTRACT

Reference Radiation for Cosmic Rays in RBE Research. (August 2010)

Shaoyong Feng, B.S., Tsinghua University

Chair of Advisory Committee: Dr. Leslie A. Braby

When astronauts travel in space, they are exposed to high energy cosmic radiations. The cosmic ray spectrum contains very high energy particles, generally up to several GeV per nucleon. Currently NASA is funding research on the effects, such as acute radiation sickness, of cosmic radiation. Animal models are used to conduct the studies of radiation effects of particles in the range of several MeV/nucleon to about 1000 MeV/nucleon. In order to compare different radiations, the biological effectiveness relative to a specific radiation is usually used. For low energy heavy ions and neutrons 250 keV photons are usually used for the reference radiation but their depth dose distribution is very different from that for cosmic rays. In this research, the advantages of using high energy electrons as the reference radiation for research on cosmic radiation were demonstrated. The conclusion is based on the evaluation of the dose distributions and microdosimetric spectra of the electrons and high energy protons as a function of depth in a tissue equivalent absorber as determined by Geant4 simulation.

ACKNOWLEDGEMENTS

I would like to thank my committee chair, Dr. Leslie Braby, and my committee members, Dr. Ford, Dr. Turner, for their guidance and support throughout the course of this research.

NOMENCLATURE

LET	Linear Energy Transfer
RBE	Relative Biological Effectiveness
ARC	Acute Radiation Syndrome
SPE	Solar Particle Event
CARR	Center of Acute Radiation Research
CSDA-range	Continuous Slowing Down Approximation-range
y	Lineal Energy
z	Specific Energy

TABLE OF CONTENTS

Page

LIST OF FIGURES

FIGURE Page

FIGURE Page

LIST OF TABLES

I. INTRODUCTION

I.A Cosmic rays

Cosmic rays are energetic particles originating from outer space that impinge on Earth's atmosphere. Cosmic radiation produced at its source is usually called primordial cosmic rays. It is modified during its propagation through galactic and extragalactic space. Cosmic rays arriving unperturbed at the Earth's atmosphere are usually called primary cosmic rays. The energy spectra of primary cosmic rays and the main charged components of the primary cosmic ray spectrum are shown in Figure I.1 and I.2. The particle intensity decreases with increasing energy. Protons are the dominant particle species (85%) followed by alpha particles (12%). Elements with a nuclear charge $Z \geq 3$ represent only a 3% fraction of charged primary cosmic rays (Grupen 2005).

Most cosmic rays have energies between 100 MeV and 10 GeV. The number of cosmic rays with energies beyond 1 GeV decreases by about a factor of 50 for every factor of 10 increases in energy. The cosmic rays have very high penetrating ability due to their high energies. The cosmic radiation can easily penetrate shielding and reach human body during space mission. So the radiation effects by high energy cosmic rays are critical to astronauts and the space mission duration that is often limited to avoid high radiation exposures. The radiation effectiveness of protons are focused on, because protons are the dominant particle species of cosmic rays.

This thesis follows the style of *Health Physics*.

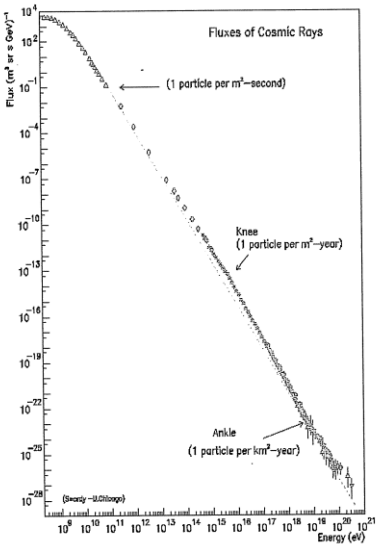

Figure I.1. Primary cosmic ray energy spectrum (Mishev et al. 2004).

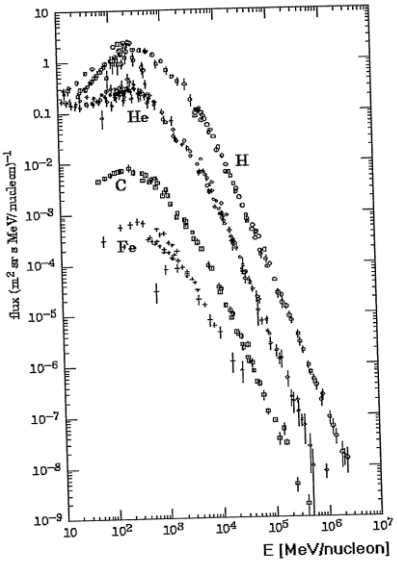

Figure I.2. Energy spectra of the main components of charged primary cosmic rays (Simpson 1983).

I.B NASA research on radiation effects

In the NASA radiation effects research program, animal model systems, such as ferrets, mice, and pigs, are being utilized to evaluate the space radiation-induced acute radiation syndrome (ARC) (National Space Biomedical Research Institute [online], 2010). Their overall aims are to determine whether adverse acute biological effects are likely to occur in astronauts exposed to the types of radiation, at the appropriate energies, doses and dose-rates, present during a solar particle event (SPE). Experiments involving the exposure of animals to radiation have been performed with all three species of animals as part of the Center of Acute Radiation Research (CARR) grant activities, and with three different types of radiation, electrons, gamma rays and protons. At this point, a tremendous amount of data has been gathered on mice, which are utilized for studies of hematopoietic cell function, immune system function and fatigue. These studies have been performed with 6 MeV electrons, Cobalt-60 gamma rays, and with 50 MeV n^{-1} protons.

It is planned that the same experiments outlined for performance in Year 1 will be performed with 50 MeV n^{-1} proton radiations for the second year of the CARR grant. Potentially, several other different proton energies representing the distribution of proton energies in a SPE (up to an energy of 230 MeV n^{-1} protons at University of Pennsylvania (Penn) or 270 MeV n^{-1} protons at the Loma Linda Medical Center (Loma Linda)) may also be performed in Year 2. In Year 3, they plan to do similar experiments as those planned for Year 1 using a full simulated SPE at NASA Space Radiation Laboratory, which will involve the addition of higher energy protons than those that are available at

Penn or Loma Linda. Studies will also be performed with a reduced weight-bearing system (the Partial G system developed at MIT by Dr. Erika Wagner) and radiation in Year 2 of the CARR grant, involving studies in mice of hematopoietic cell counts and immune system parameters.

Overall, the NASA research group plans to conduct the research on lower energy particles first and then increase the energy of the radiations to better simulate the cosmic ray radiations. In the second year, the radiation utilized on the research project is up to 270 MeV for protons which is in the range of 100MeV to 10GeV of the most common cosmic rays. For further research, they will focus on higher energy particles. It is important to find a reference radiation that provides a similar energy distribution as the high energy cosmic rays in the human body in order to evaluate the relative biological effectiveness (RBE) of the cosmic rays.

I.C Relative biological effectiveness and microdosimetry

The influence of radiation quality on biological systems is usually quantified in terms of RBE. The RBE is defined, for a specific radiation (A), as: RBE(A)= Dose of reference radiation required to produce a specific level of response divides by Dose of radiation A required to produce an equal response, with all physical and biological variables, except radiation quality, being constant (Rossi and Zaider 1996). According to the equation, the RBE depends on the reference radiation and the particular biological effect involved in the research. For radiation protection purpose, the radiation weighting factor is related to the RBE which is assumed to be a function of radiation quality,

expressed in terms of linear energy transfer (LET). More specifically, in many systems the RBE increases with LET to a maximum near an LET of 100 keV μm^{-1} and then declines (NCRP 1990). In most systems, 250 keV photons are used as the reference radiation.

The mechanics of radiation effects are too complex to be understood completely. The interaction of ionizing radiation with matter is invariably followed by complicated chain of processes. Thus the chemical consequences of radiation of even a simple substance such as pure water are still not entirely defined. The average energy absorbed per unit mass of irradiated medium, the absorbed dose, is often used as an indicator of the biological effectiveness. While the absorbed dose is a useful and standard quantity in the specification of irradiation, effects often depend on the pattern in which a given amount of energy is deposited in the irradiated area as well as the size of the area irradiated. Microdosimetry is the systematic study and the quantification of the spatial and temporal distribution of absorbed energy in irradiated matter (Rossi and Zaider 1996).

Radiation biology is concerned with targets that range in size over at least 10 orders of magnitude between biomolecules and tissues of whole organisms. Most of the effects are ultimately due to DNA damage but in addition to their number the spatial distribution of the affected molecules is of cardinal importance in the causation of effects. The utility of microdosimetry in the interpretation of biological effects in terms of radiation physics is generally restricted to cellular effects. The equivalent diameter of

sites for the detector used in microdosimetry is generally between 1 to 20 μm, because the diameter of mammalian cells is of the order of 10 μm.

In this study, the microdosimetric characteristics of electrons and protons were investigated with the objective of using electrons as the reference radiation for cosmic rays. Microdosimetry research, to make predictions of RBE for low-energy X-rays and low-energy fast neutrons, was conducted previously (Cucinotta et al. 1991). And in recent studies, Geant4 (Agostinelli et al. 2003) toolkits were used to simulation the solar protons within a spacecraft in microdosimetric view (Wroe et al. 2005)

II. MODELS AND METHODS

II.A Properties of high energy protons

Simply, the interactions and properties of protons in water, which makes up about 60% of the body weight, are discussed below. The stopping power and range of protons in water are listed in the following tables (Table II.1 and Table II.2). The range of 1000 MeV protons in water is about 325 cm. For 850 MeV protons, the CSDA range (continuous slowing down approximation-range) is about 259 cm. The estimated energy left when 1000 MeV protons travel through human body is about 850 MeV (Using 60 cm as the diameter, reasons shown in the next paragraph). As shown in Table II.1, the stopping power changes only from 2.3 MeV $cm^2 g^{-1}$ to 2.1 MeV $cm^2 g^{-1}$ for protons from 850 MeV to 1000 MeV. So, generally, the dose for 1000 MeV protons in the human body will be quite uniformly distributed.

The 250 keV photons, which are used as the reference radiation in most systems, would be inappropriate for the RBE of cosmic rays, due to their rapid attenuation in the human body. In order to be used as the reference for the cosmic rays, the radiation should exhibit the following properties: a) the range would be greater than the diameter of the human body (use 60cm as the diameter of a typically man according to the size of the reference man in ICRP (ICRP 1975)), and b) the stopping power along the range would not change significantly.

Table II.1. Stopping power and range of protons in liquid water (Berger et al. 1998)

Kinetic energy (MeV)	Stopping Power (MeV cm^2 g^{-1})			Range		
	Electronic	Nuclear	Total	CSDA ($g\ cm^{-2}$)	Projected ($g\ cm^{-2}$)	Detour Factor
8.00×10^2	2.33	4.08×10^{-4}	2.33	2.37×10^2	2.37×10^2	0.9992
8.50×10^2	2.30	3.85×10^{-4}	2.30	2.59×10^2	2.59×10^2	0.9992
9.00×10^2	2.26	3.65×10^{-4}	2.26	2.81×10^2	2.81×10^2	0.9992
9.50×10^2	2.24	3.46×10^{-4}	2.24	3.03×10^2	3.03×10^2	0.9992
1.00×10^3	2.21	3.30×10^{-4}	2.21	3.25×10^2	3.25×10^2	0.9992

Table II.2. Stopping power of electrons in liquid water (Berger et al. 1998)

Kinetic Energy (MeV)	Stopping power (MeV cm^2 g^{-1})					
	Collision	Radiation	Total	CSDA Range ($g\ cm^{-2}$)	Radiation Yield	Density
6.00×10^1	2.16	1.40	3.56	2.28×10^1	2.22×10^{-1}	6.09
7.00×10^1	2.17	1.66	3.83	2.55×10^1	2.50×10^{-1}	6.38
8.00×10^1	2.18	1.91	4.10	2.80×10^1	2.75×10^{-1}	6.64
9.00×10^1	2.19	2.17	4.37	3.04×10^1	2.98×10^{-1}	6.87
1.00×10^2	2.20	2.43	4.64	3.26×10^1	3.19×10^{-1}	7.08
1.25×10^2	2.22	3.09	5.31	3.76×10^1	3.66×10^{-1}	7.52
1.50×10^2	2.24	3.75	5.99	4.20×10^1	4.06×10^{-1}	7.88
1.75×10^2	2.25	4.41	6.66	4.60×10^1	4.40×10^{-1}	8.18
2.00×10^2	2.26	5.08	7.34	4.96×10^1	4.70×10^{-1}	8.45
2.50×10^2	2.28	6.42	8.70	5.58×10^1	5.19×10^{-1}	8.89
3.00×10^2	2.30	7.76	1.01	6.12×10^1	5.58×10^{-1}	9.25

In this project, the 300 MeV electrons were investigated to determine their usefulness as the reference radiation for the research on cosmic radiation. The CSDA

range of 300 MeV electrons is 61.5 cm in water, which is just a little larger than the diameter of the human phantom. However as electrons would not travel exactly along the diameter, the range is sufficient for the research. Using the average cord length 40 cm (two thirds of the diameter) as the average path length of electrons in the body, the electron energy would be about 60 MeV when exiting. The collision stopping would range from 2.3 MeV cm^{-1} to 2.16 MeV cm^{-1} (Table 2), which is almost identical to the stopping power range for protons. So the dose distribution would be similar to that of 1000 MeV protons.

II.B Geant4 Models

In this project, the dose distributions and secondary particles generated by 300 MeV electrons and 1000 MeV protons are compared first to determine the feasibility of using the electrons as the reference radiation for determines proton RBE. Then the microdosimetric spectra of the electrons and the protons were studied. Geant4 was used to perform the Monte Carlo simulation. A cylindrical phantom with a 60 cm diameter and 1 m in height was utilized to simulate a reference man model as discussed in the ICRP report (ICRP 1975). Water was used as the construction material to simplify the model and to reduce the simulation time.

The initial direction of the primary electrons and protons was parallel to the X axis as shown in Figure II.1. The primary and the secondary particles do not travel very far in the Z direction, so a 1 m tall cylinder is appropriate for the project. The whole phantom was put in vacuum, which does not significantly affect the results relative to

being in air. The small difference between in air and in vacuum is primarily the buildup of secondary electrons in the very thin surface layer of the phantom. The difference is comparable with the statistic error of the results, but setting the phantom in vacuum has the advantage of accelerating the calculations. The sources were placed outside of the phantom. The coordinates used in this paper are all according to the geometry in the Figure II.1.

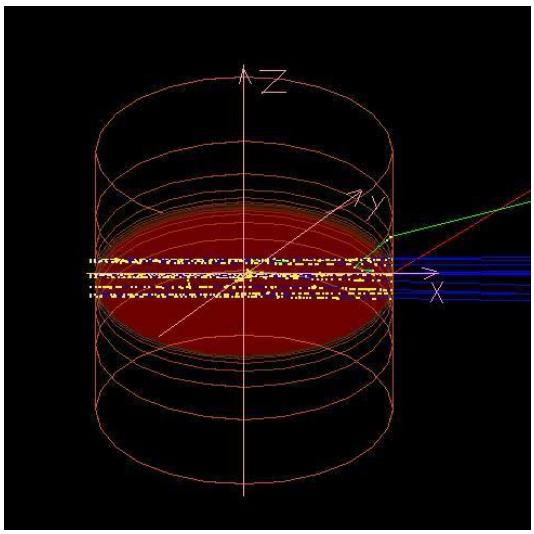

Figure II.1. The geometry of phantom and primary particles. In the figure, the primary particles are 1GeV protons. The layers of the detector with different cut values are used to reduce simulation time. (Generated by Geant4)

Most of the research focused on the dose distribution, secondary particles and microdosimetric dose distribution in a thin layer locating at Z=0mm (the red layer in Fig. II.1). To simulate all radiations that could induce energy deposited in the layer, a very large beam was used. A 60 cm square beam covering from z=-30cm to z=30 cm and

from y=-30cm to y=30 cm is used for dose distribution and secondary particle simulations. In the simulations of the microdosimetry, a much smaller size beam was used to reduce the simulation time (see Appendix A). Considering that the dose deposited by the particles originating from the parts that is far away from the layer is negligible, using a smaller beam size does not affect the results.

The project was divided into three parts. In the first part, the dose distribution was studied to investigate the suitability of 300 electrons as the reference radiation. In the second part, the secondary particle energy distributions in different parts of the phantom were studied to investigate how variations in radiation spectrum might influence the use of electrons as the reference radiation for research on the cosmic radiation. In the third part, the microdosimetric distributions in several parts of the human body were studied. As discussed in the introduction, microdosimetry is an important method to describe RBE.

III. DOSE DISTRIBUTION

In order to act as the reference radiation for RBE research of the cosmic rays, the reference radiations should have similar dose distributions in the human body. This would prevent biological effects due to differences in the ratio of doses throughout the human body.

In ordinary RBE research, the 250 keV photons are utilized as the reference radiation. Photons are effective for most systems, because the investigations are mainly interested in the radiation effects in a thin layer of tissue or bacteria. As the sample layer is thin, the dose can be considered uniformly distributed for all kinds of radiation. So the 250 keV photons are appropriate for these systems.

When researching the radiation effects of the cosmic rays on the human body, however the 250 keV photons are inappropriate. The range of cosmic rays is very large, so all of the human body can be irradiated as the cosmic rays can easily travel through. But for 250 keV photons, the attenuation in the human body is significant. Dose decreases to less than 50% at the depth of several centimeters. So, it is critical to find an appropriate radiation to serve as the reference radiation for the RBE research for the cosmic rays. In this part, the dose distributions of 1000 MeV protons, 300 MeV electrons, and 250 keV photons in a thin layer of phantom locating between z=-2.5 mm to z=2.5 mm were studied (see Fig.III.1).

III.A Dose distribution of 1000 MeV protons

Figure III.1 shows the dose distribution of protons in the 5 mm thick layer which is centered at z=0 of the human phantom. In the figure the dose is a little higher on the left part which is close to the radiation source, and a little lower on the right part. Figure 2.2 shows the relative dose along the X axis. At the entrance to the phantom, the dose is a little low relative to the maximum (at x=-300 mm, it is 95% of the maximum). The dose reaches its highest value at only several millimeters depth in the phantom, and then drops gradually with increasing depth. The dose at the exit areas is about 10% lower than the maximum dose, so the degree of difference is not very large.

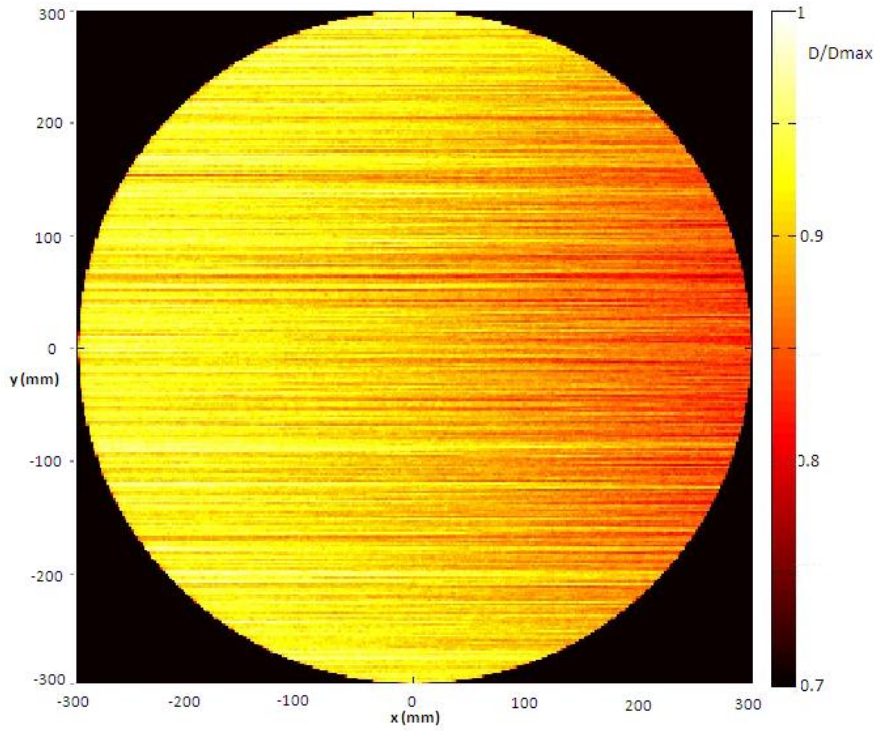

Figure III.1 Dose distribution of 1000 MeV protons. The dose was measured in the thin layer centering at z=0 mm.

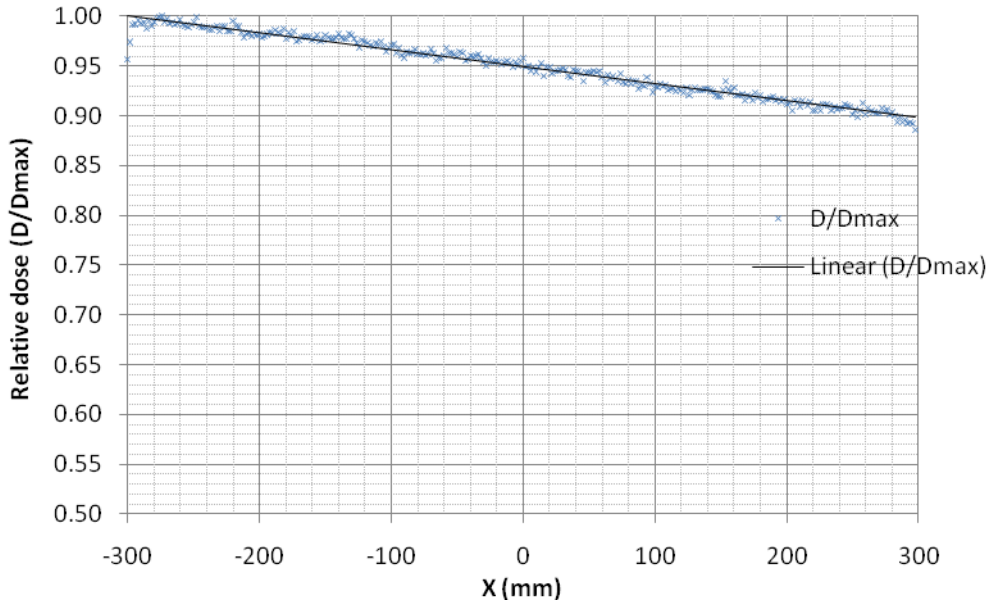

Figure III.2 Relative dose of 1000 MeV protons along the X axis. The linear trend line is also added in the figure.

III.B Dose distribution of 250 keV photons

For the 250 keV photons, which are used as reference radiation in most systems, the dose distribution is shown in Figure III.3. Figure III.4 provides the relative dose to the maximum value along the X axis to show the detailed distributions. The dose reaches the maximum value at about 5 mm in the depth and then drops quickly with the increasing depth. At 20 mm depth, for which x=-280 mm, the dose is only 70% of the maximum. So the photon is only useful for research on thin layer tissues, and should not be used in the research on RBE of cosmic rays.

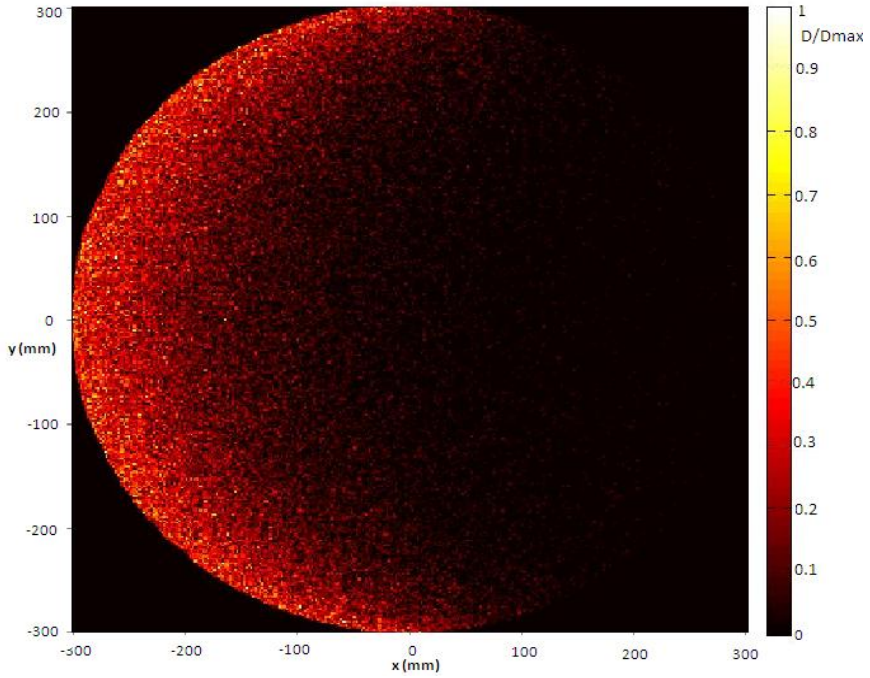

Figure III.3 Dose distribution of 250 KeV photons. The dose was measured in the thin layer centering at z=0 mm.

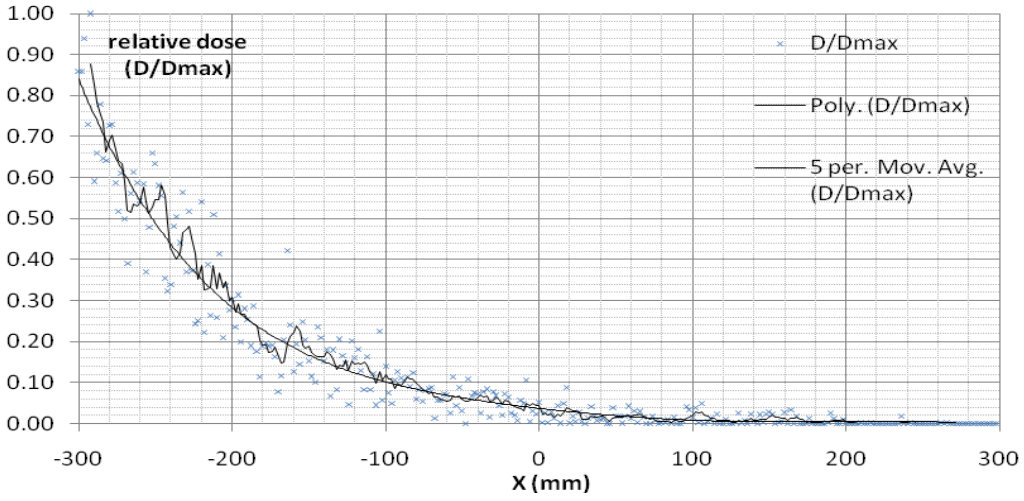

Figure III.4 Relative dose of 250 KeV protons along the X axis. The polynomial trend line and a trend line with 5 point moving average are shown in the figure.

III.C Dose distribution of 300 MeV electrons

The dose distribution of 300MeV electrons in the sample phantom is shown in Figure III.5. The dose is lower in the primary particle entrance and exiting areas of the phantom but higher in the center, which is different from the dose distribution of protons. In the edge of the phantom, more delta rays are scattering out than scattering in, so the dose is lower than that in the center.

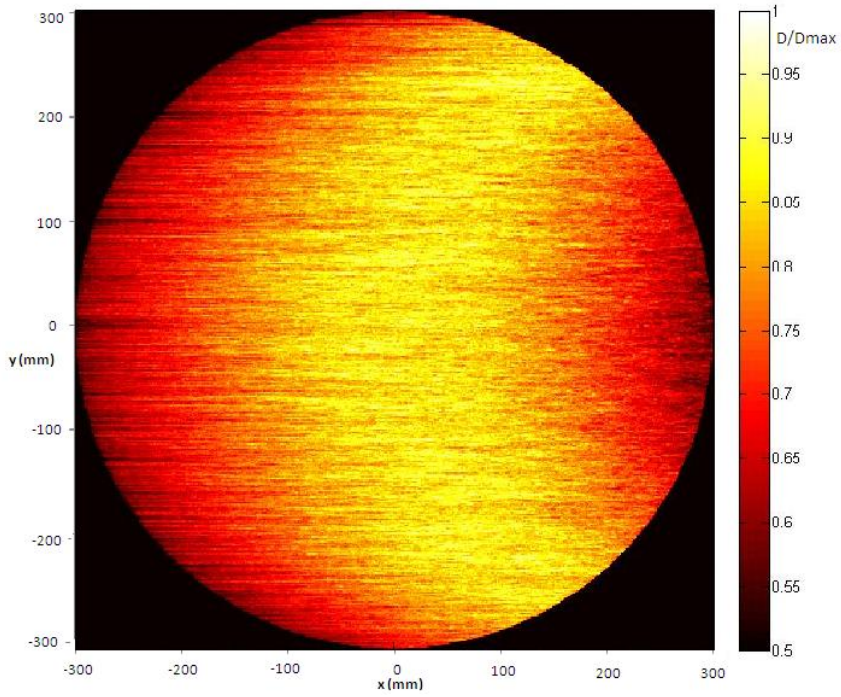

Figure III.5 Dose distributions of 300MeV electrons. The dose was measured in the thin layer centering at z=0 mm.

Figure III.6 shows the relative dose (relative to the dose in the center of the phantom, where the dose is highest) distribution along the X axis. The dose in the

entrance area is only 75% of the maximum values, and it is about 70% of the maximum value in the exiting area. The differential is about 30%.

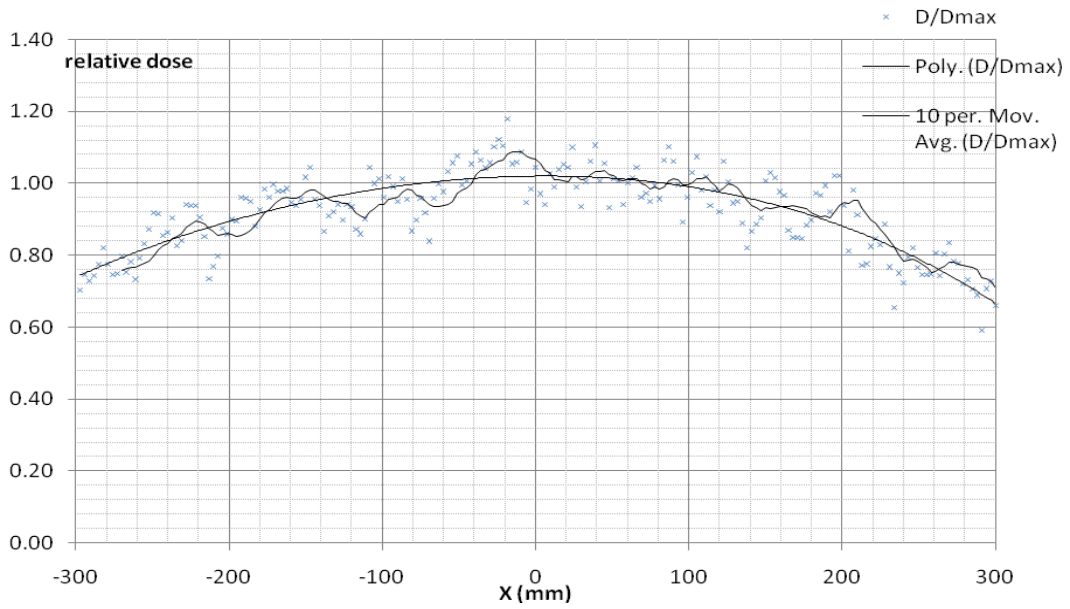

Figure III.6 Relative dose along X axis for 300 MeV electrons. The points in the figure are dose relative to the value averaged over x=-20mm to x-20mm where the dose is largest. Along the X axis, 300 sample points are used. In the figure, both the moving average curve and a polynomial trend line are provided.

IV. SECONDARY PARTICLES

The secondary particle spectrum is an important concern in the RBE study. The study of the spectrum of the secondary particles provides more information about the primary particles than the dose distribution, and helps with the study of the microdosimetric distributions. For high energy protons and electrons, a large portion of energy is deposited in the absorber in the form of secondary electrons, so the spectrum of the secondary electrons reflects the patterns of energy deposited. In this part, the initial energy of first generation secondary electrons of 1000 MeV protons and 300 MeV electrons is studied. Several sample areas with a diameter of 10 mm are selected along X axis to study the distributions at depths of the phantom. The probability density f(E), is the probability function of the initial energy of the first generation secondary electrons generated in the sample areas.

IV.A Initial energy spectra of the first generation secondary electrons of 100MeV protons

Figure IV.1 shows the energy spectra of the initial energy of secondary electrons of 1 GeV protons in several parts of the phantom. One more figure is also provided with the curves from different parts plotted in a single picture (Figure IV.2). The energy distributions of secondary electrons in different parts of the phantom are similar. In the figures, the highest energy threshold for secondary electrons is about 3.5 MeV, and the threshold is lower in the deeper part of the phantom. Theoretically the highest energy of

secondary electrons generated by 1000 MeV protons is 3.34 MeV, and the highest energy decreases with the energy of protons (Attix 2004).

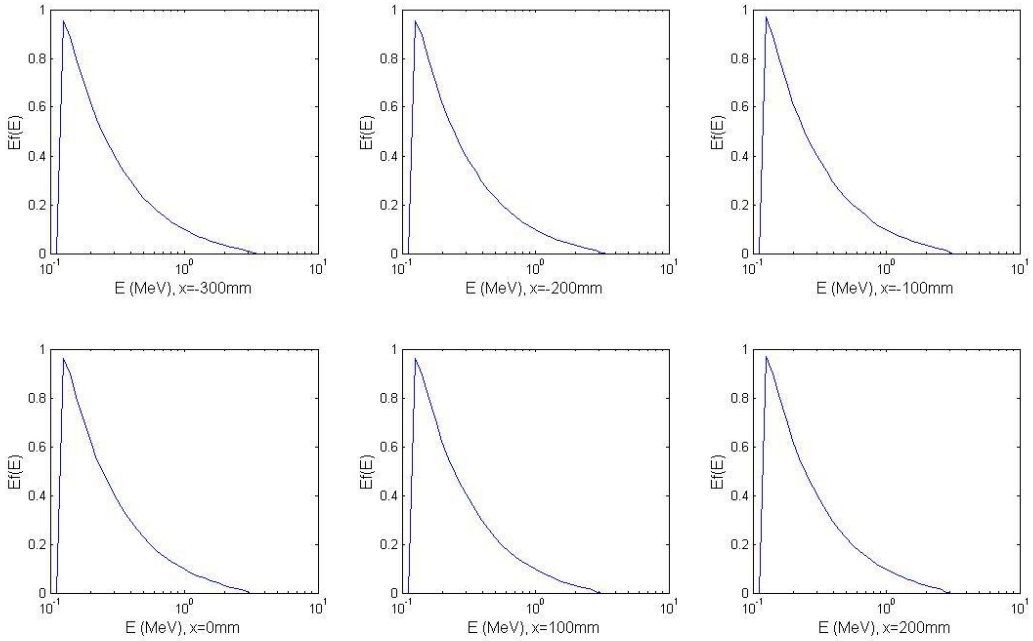

Figure IV.1.Energy spectra for secondary electrons of 1 GeV protons. The coordinates are in the center of the sample areas. As the sample areas are along X axis, only x values are shown.

The highest energy that is obvious in the figures of the secondary electrons is a little smaller in the part of the phantom that is farther from the source compared with that of the closer part of the phantom (see the following Figure IV.2). It is 3.34 MeV for x=-300 mm which is the surface part of the phantom facing the proton source and about 3 MeV for x=300 mm which is the furthest part from the source. The initial energy of

the primary protons is 1000 MeV, and the energy would go down by about 150 MeV to 850MeV when the protons exit the phantom (when travelling about 50-60 cm in path). Theoretically, the maximum energy of secondary electrons is 2.9 MeV for the 900 MeV primary protons. The energy of the secondary electrons does not change a lot. In Figure IV.2, no other differences can be seen between the energy spectra in different depth of the phantom.

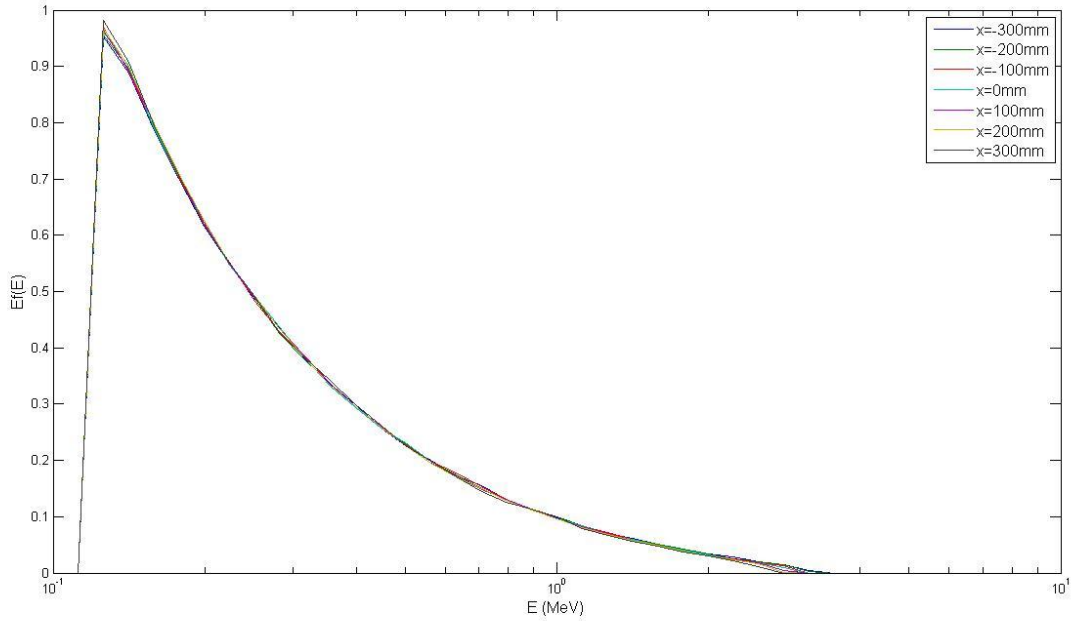

Figure IV.2. Comparison of energy spectra of secondary electrons of 1 GeV protons at different depths in the phantom.

IV.B Initial energy spectra of first generation secondary electrons of 300 MeV electrons

As discussed above, the largest energy of secondary electrons that is visible in the Ef(E) plot for photons is about 3 MeV. Since 300 MeV electrons produce secondary electrons up to 150 MeV. If the initial energy spectrum of first generation secondary electrons of 300 MeV is compared with the spectrum of the protons, no meaningful information would be given as they are in different energy range. So in order to better compare the results of electrons with protons, only secondary electrons less than 3 MeV are recorded. If the energy of secondary electrons was larger than 3 MeV, they were still simulated and the secondary electrons with energy less than 3 MeV were recorded. In this way, all spectra would reflect the distribution of secondary electrons less than 3 MeV electrons.

The simulation results are shown in Figure IV.3 and IV.4. The geometry of the detectors was the same as that used for studying protons. There is a sharp edge at 3 MeV in the right end of the curve because only secondary electrons with energy less than 3 MeV were recorded.

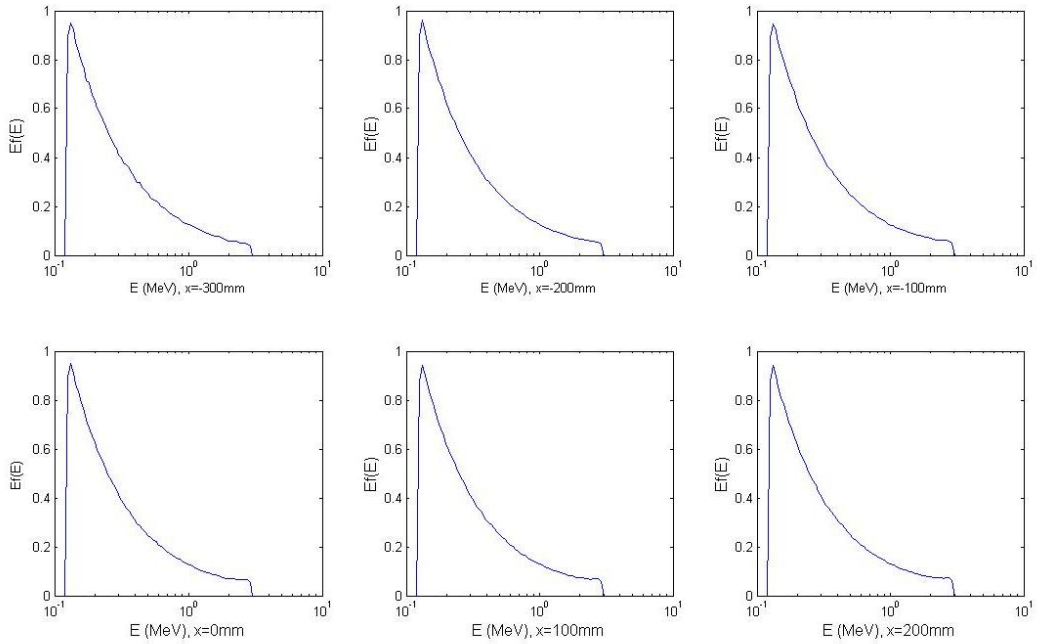

Figure IV.3.Initial energy spectra of the first generation secondary electrons (no more than 3 MeV) of 300 MeV electrons.

In figure IV.4, all spectra from different depths of the phantom are plotted together. The spectra in different depths of the phantom are almost identical except that the probability function is a little larger in the low energy range at the position closer to the radiation source relative to the further positions. But the difference is very small.

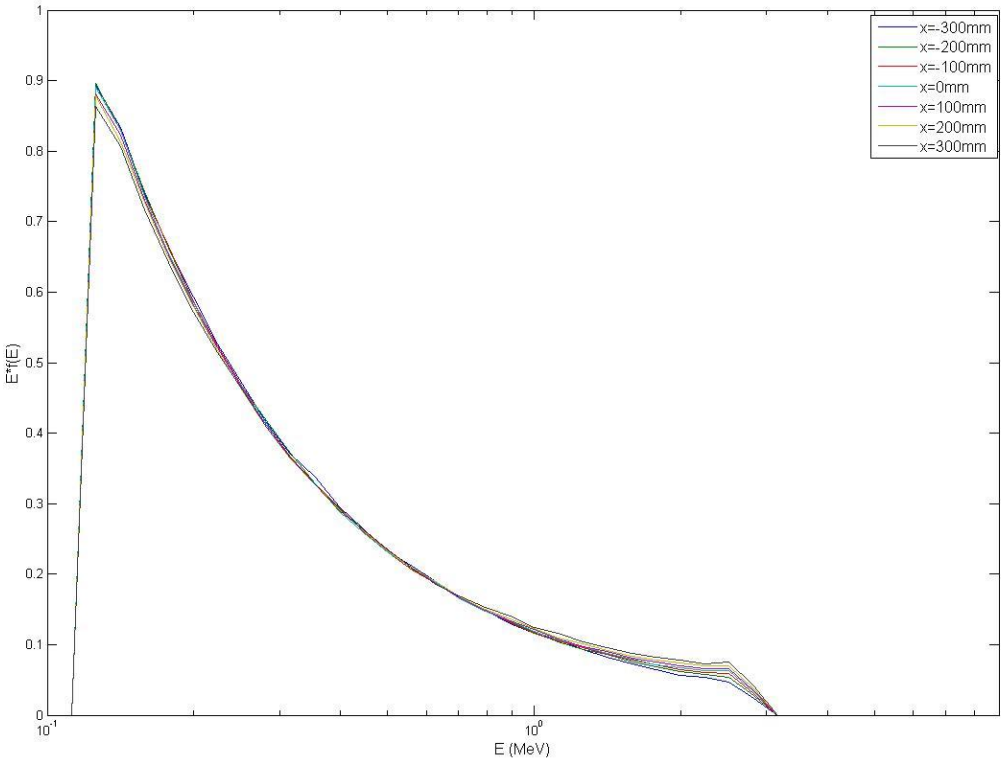

Figure IV.4. Comparison of energy spectra of secondary electrons of 300 MeV electrons at different depths in the phantom.

IV.C Comparison of the secondary electron spectra of 300 MeV electrons and 1 GeV protons

Figure IV.5 shows the secondary electron energy spectra from 300 MeV electrons and 1 GeV protons. In the low energy range (below 0.5 MeV), the curves from the two different primary particles are almost identical. But for higher energy, the curves for 300 MeV electrons show larger probability of secondary electrons. The first generation secondary electrons of 300 MeV primary electrons can be up to 150 MeV, so

there is a sharp drop rather than gradually decrease to zero in the curve as just the secondary electrons with energy lower than 3 MeV were recorded.

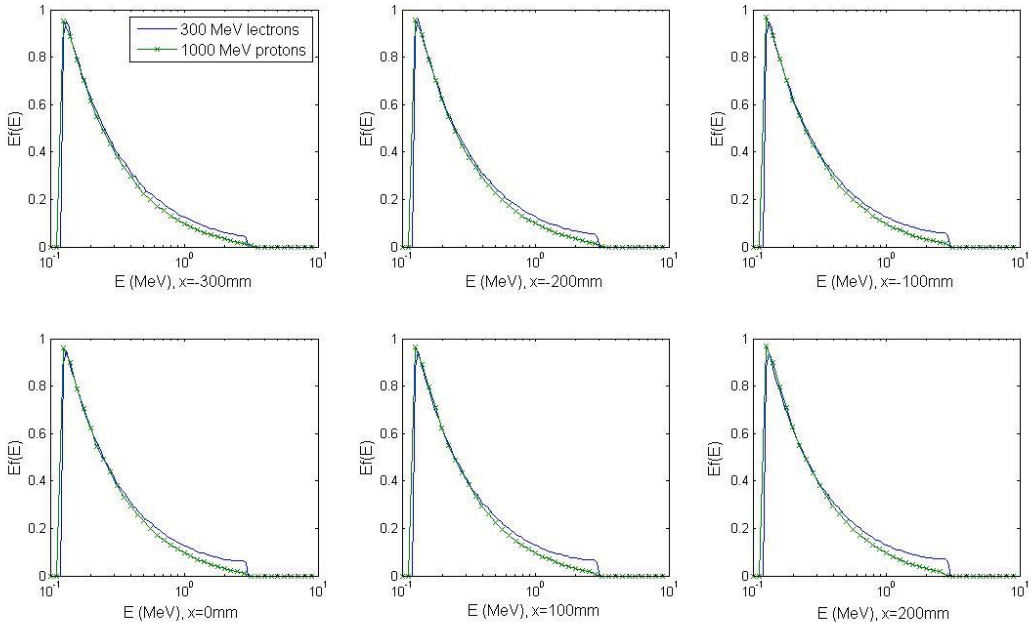

Figure IV.5. Comparison of energy spectra for secondary electrons of 1 GeV protons and 300 MeV electrons.

V. MICRODOSIMETRIC DOSE DISTRIBUTION

As discussed in Section I, the diameter of mammalian cells is of the order of 10 μm. In the simulation 8 μm was used as the diameter of detector site for collecting the microdosimetric dose distribution data. There are two principle quantities in microdosimetry: specific energy, z, and lineal energy, y, defined as follows (ICRU 1980).

The specific energy, z is the quotient of ε by m, where ε is the energy imparted by ionizing radiation to matter of mass m:

$$z = \frac{\varepsilon}{m} \tag{1}$$

The linear energy, y, is quotient of ε by $\bar{l}$, where ε is the energy imparted to the matter in a volume of interest by an energy deposition event, and $\bar{l}$ is the mean chord length in that volume:

$$y = \frac{\varepsilon}{\bar{l}} \tag{2}$$

The function f(y) is used to describe the distribution of y. The probability that the lineal energy produced by an event is in the interval [y, y+dy] is f(y)dy. So the expected dose delivered by an event is in the interval [y, y+dy] is: d(y)=y f(y)dy.

In microdosimetry, yf(y) versus y and yd(y) versus y are always plotted in a semi-log representation. So the area under the curve delimited by any two values of y is

proportional to the frequency of events (for yf(y) versus y plot) or fraction of dose (for yd(y) versus y plot) delivered by events with lineal energies in this range (Rossi and Zaider 1996).

In microdosimetry, the diameter of the detector has significant effects on the results, especially for the low energy secondary particles. To demonstrate the affects, a series of simulations using 20 μm diameter detectors were conducted to compare with the results with detector of 8 μm.

Generally, Geant4 needs a cut value and particles are considered to be stopped at the point where the energy or the range of the particles meets the criteria. Decreasing the cut value generally improves the accuracy of the calculation but it also increases the calculation time. A reasonable cut value must be determined for the simulation. If the cut value is set too large, the results will not reflect the microdosimetric distributions but the average stopping power of a long path. On the other hand, if the cut value is set too small, the simulation time will be dramatically increased. The Monte Carlo simulation is time consuming, thus efficiency is an important issue when running a large number of simulated particle tracks. In order to study the effects of the cut value on the results, simulations of using ½ of the detector diameter and ¼ of the detector diameter as the cut value were compared.

In the simulation, several locations in the phantom for evaluation of results are selected in order to better compare the microdosimetric distributions of protons and the reference electrons. The selected locations are uniformly distributed on the following three lines: Y=0 cm, Y=15 cm and Y=25 cm as shown in Figure V.1. For each sample

area, the diameter is 0.1 mm and hundreds of detectors are put in the area. The original particles are coming from the left to the right, parallel to the X axis, see II.C.

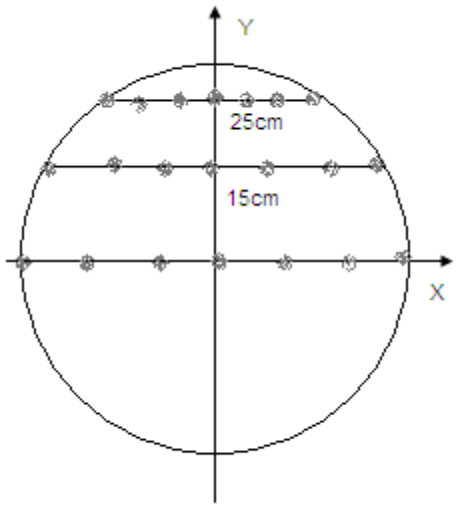

Figure V.1. Sample areas for collecting microdosimetric distribution data.

V.A 1000 MeVprotons

In this part, the microdosimetric distributions of 1000 MeV protons at different positions of the phantom are discussed. Also the effects of the cut value and the site size on the results are described.

V.A.1 Microdosimetric spectra at different positions of the phantom

The following figures show the microdosimetric distributions for 1000 MeV protons at different depths in the phantom. In Figure V.2, the dose spectra are plotted individually to show the detail of every single sample point. In Figure V.3, the spectra are plotted together to study the difference and similarity at different depth of the

phantom. In the simulation, the diameter of detectors is 8 μm and the cut value is 2 μm for all kinds of particles.

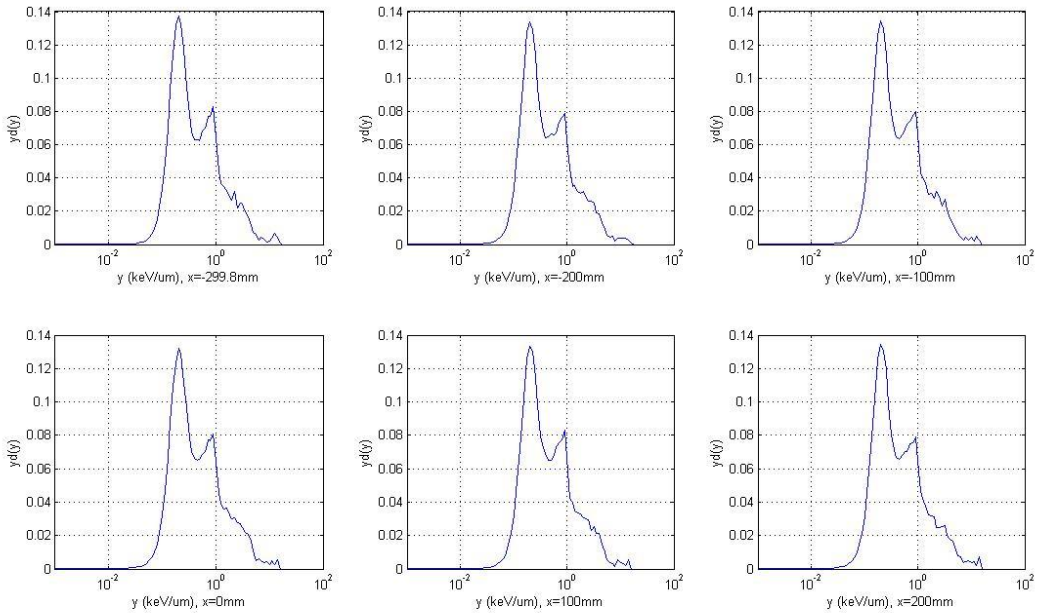

Figure V.2. Microdosimetric distributions for 1000 MeV protons at different depths in the phantom in the representation of d(y). Coordinates shown in the figure are in millimeters. The sample points are on the Y=0 cm line, so in the figure the coordinates just show the x values as the y and z values are 0.

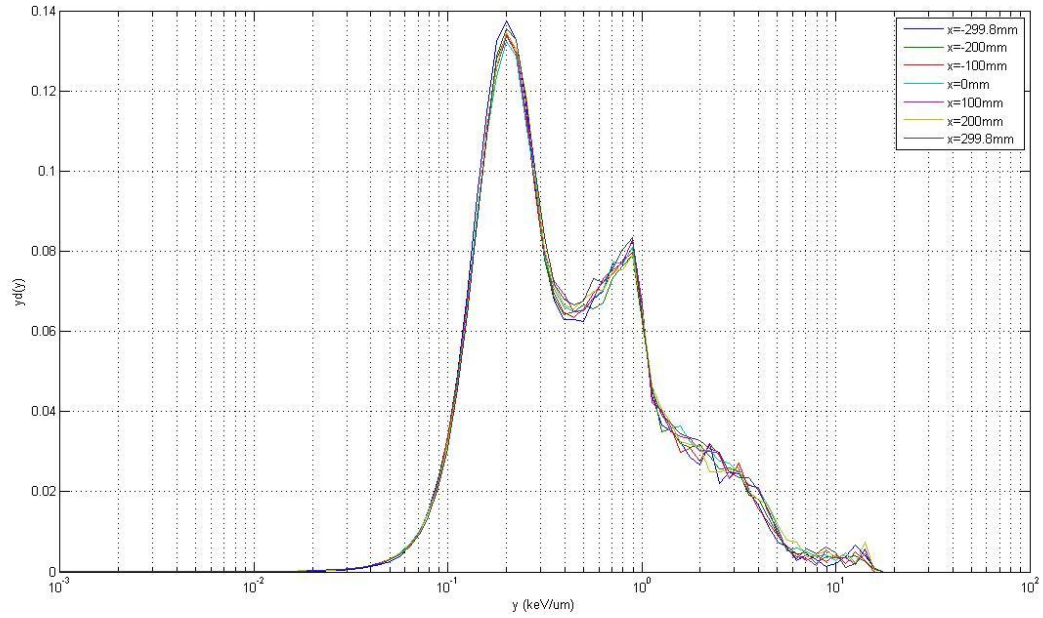

Figure V.3 Microdosimetric distributions for 1000 MeV protons at different depths in the phantom. The sample points are the same as in Figure V.2.

As shown in Figure V.2 & V.3, the patterns of the curves from different parts of the phantom are almost identical. There are several peaks located at y=0.2 keV μm^{-1}, 0.9 keV μm^{-1}, and between 10-20 keV μm^{-1}, respectively. Also there is a continuous decreasing part from 1 keV μm^{-1} to about 6 keV μm^{-1} for all sample areas. The first two peaks contribute most to the dose due to their high probability (the dose is proportional to area covered by the curve). But the biological effects depends more on the events with higher y values, because the high density of the ion-pairs along the path of the radiation.

V.A.2 Microdosimetric spectra at different cut values

As discussed before, the cut values affect the precision and the time required for the Geant4 simulation. In this part, the results of simulations with a cut value of 4 μm, which is ½ of the diameter of the detector, with the results before, for which the cut value is 2 μm, ¼ of the diameter of the detector, are studied. The microdosimetric dose distributions in several parts of the phantom are shown in Figure V.4. The microdosimetric distribution does not change a lot at different depths in the phantom, which is similar to the results with a cut value of 2 μm. There are three main peaks in every curve, centering at 0.1 keV μm^{-1}, 0.9 keV μm^{-1}, and locating between 10 keV μm^{-1} and 20 keV μm^{-1}, respectively (or several peaks in this range), and a continuously slowing down part between 1 to 10 keV μm^{-1}.

In Figure V.5, the microdosimetric dose distributions obtained with the cut value of 2 μm and 4 μm are compared. The patterns and features of the two curves are almost identical. The main peaks in the curves are located in the same range. For the peak centering at 0.9 keV μm^{-1} seems shifting a little right in 4 μm cut value spectrum. Also, the dose distribution in the range between y=0.3 keV μm^{-1} to 0.8 keV μm^{-1} for the cut value of 4 μm is a little lower than the 2 μm one. But in the range above 1 keV μm^{-1}, there are no difference shown in the curve partly because the statistic errors play a significant role due to the small number of events in this range.

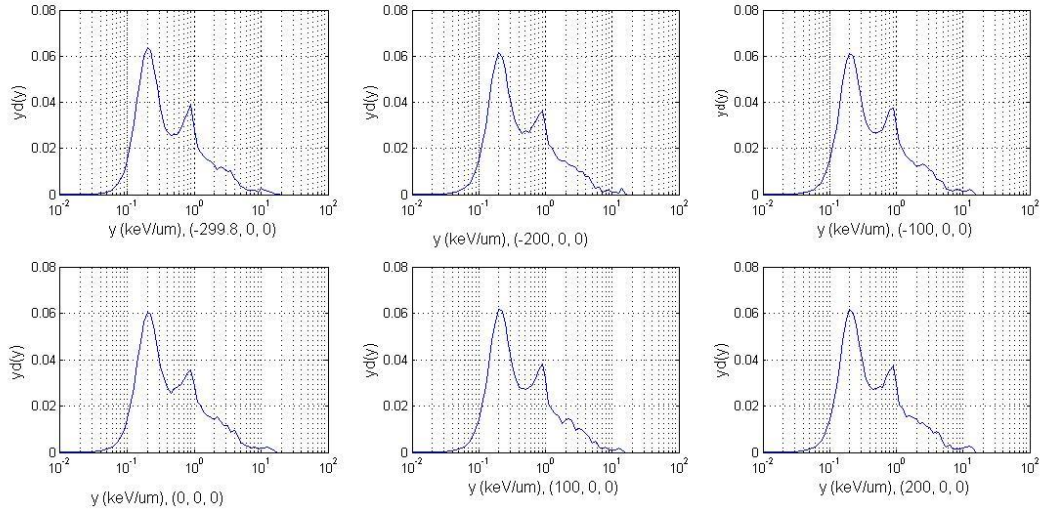

Figure V.4. Microdosimetric spectra at different depths in the phantom with a cut value of 4 μm. In the simulation the diameter of the detectors is 8 μm.

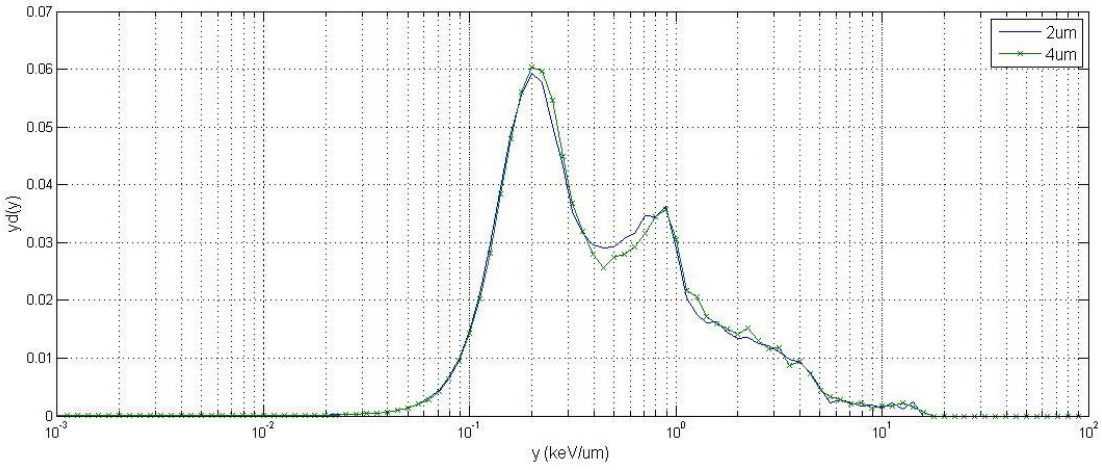

Figure V.5. Microdosimetric spectra with a cut value of 2 μm and 4 μm of 1000 MeV protons. The coordinate of the sample area is (0 mm, 0 mm, 0 mm).

V.A.3 Microdosimetric spectra at different site sizes

Figure V.6 shows the microdosimetric dose distributions with the detector diameter of 20 μm at different depths in the phantom. The spectra do not change a lot with the depth. There are two main peaks in all spectra, one centering at 0.2 keV μm^{-1}, and the other centering at 0.5 keV μm^{-1}. The spectra drop down sharply from 0.5 keV μm^{-1} to 0.9 keV μm^{-1}, and then go down slowly ending at about 20 keV μm^{-1}.

In Figure V.7, the microdosimetric spectra with detectors with the diameter of 8 μm and 20 μm are plotted in a single picture to study the affects of the detector diameter on the results. As discussed above the spectra do not show significant differences at different depths, so only data from the center part of the phantom are used to compare the distributions. Both curves show two main peaks and a long tail ending at about 20 keV μm^{-1}. But the positions of the second peak are quite different, it is centering at 0.5 keV μm^{-1} for "d=20 μm" spectrum but at 0.9 keV μm^{-1} for "d=8 μm" spectrum. Secondly, the fraction of the dose in the peak centering at 0.2 keV μm^{-1} is much higher in the "d=20 μm" spectrum than that in "d=8 μm" spectrum.

Broadly speaking, the effects of the diameter of the site size on the results are reflected in several aspects of the d(y) distribution. First, the peak with highest y values may shift a little left due to the range of particles contributing to the peak being large comparable with the small diameter, but small comparable with the large diameter. This does not necessary happen to the peaks at largest y value but depends on the stopping power of the low energy particles and their contribution to the peaks. Second, the curves

can be smoothed with a large diameter because some the rate of energy transfer is averaged over longer chord lengths.

The peak centering at 0.9 keV μm^{-1} (for d=8 μm) is mainly due to very low energy delta rays, for which the CSDA range is of the order of 8 μm. The energies deposited in the two different detectors are the same but the average cord length used to calculate the linear energy transfer for 20 μm diameter detectors is 2.5 times of the 8 μm detectors. So the peak would shift left for the 20 μm diameter detector case.

Another significant difference shown in the figure lies in the LET range of 1.0 keV μm^{-1} to 20 keV μm^{-1}. For the d=20 μm spectrum, it seems like a uniform part going down gradually. But for the d=8 μm spectrum, there are two parts: a continuum from 1 keV μm^{-1} to 5 keV μm^{-1} following by several small peaks ranging from 10 keV μm^{-1} to 20 keV μm^{-1}. One possible explanation is the statistic problem: there are fewer events in the high stopping power range compared to the low energy range. Thus in order to show details of the spectrum at the high stopping power range clearly, a large amount of events should be collected. In the simulation, less data was collected for the d=20 μm case, as it is used only for studying the effects of the diameter of the detector on the microdosimetric results to prove that the diameter is good for the research. In addition, to draw the end part of the spectrum in a reasonable way to reflect the character of the spectrum, some statistic methods have to be applied to smooth the curve. As shown in the figure, the Y axis is "yd(y)", which means $y^2f(y)$" (see page 25), so a single event in the high stopping power range would create a bin as tall as thousands of events in the low energy range due to the high y value. As a result, the step length selected to plot the

spectrum also has a significant effect on the high stopping power range of the spectrum, depending on the number of data events collected.

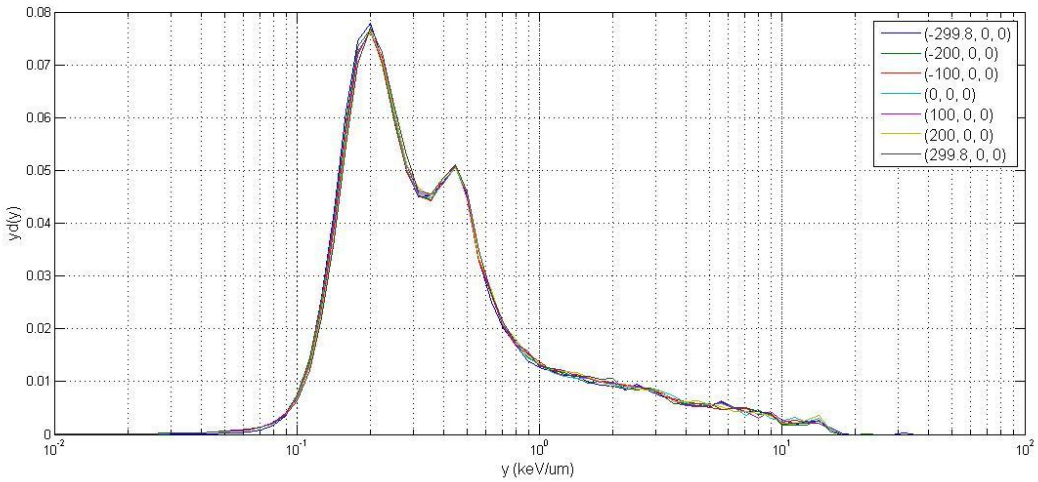

Figure V.6. Microdosimetric distribution spectra at different depths in the phantom with the detector diameter of 20 μm. In the simulation, the cut value is 2 μm which is the same as it is used in the original simulation.

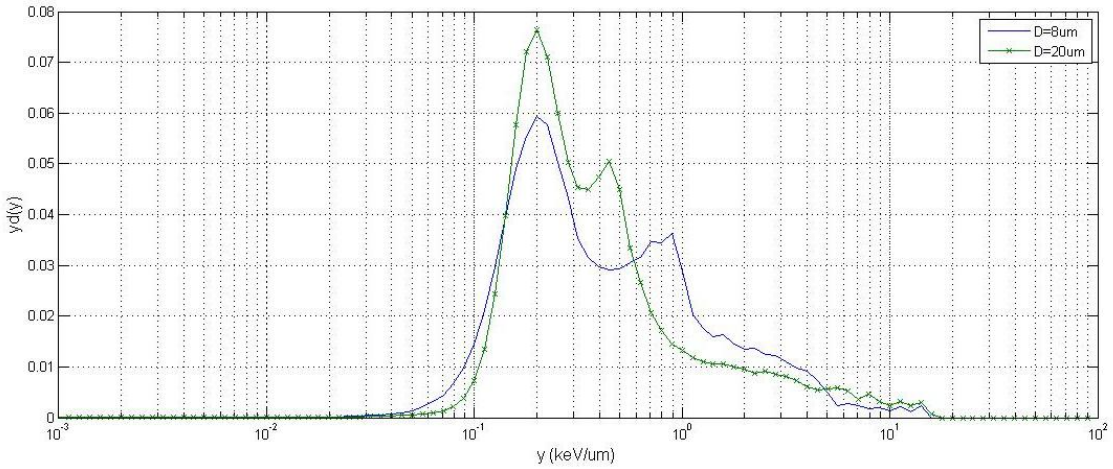

Figure V.7. Comparision of microdosimetric distribution of different site sizes for electrons.

V.B 300MeV electrons

The microdosimetric dose distribution for the reference radiation, 300 MeV electrons is studied and analyzed in this part. Comparing with 1000 MeV protons, electrons are more easily scattered, so the dose distribution is slightly different between the radiations as discussed in Section III. In the study of microdosimetric dose distribution for electrons, the same Geant4 models were used with the same detector diameter and the same cut values.

V.B.1 Microdosimetric spectra at different positions of the phantom

Figure V.8 to V.10 show microdosimetric distributions of 300 MeV electrons in several positions in the phantom, with the detector diameter of 8 μm and ¼ of the

diameter of the detector as the cut value. The sample points are the same as shown in Figure V.1.

All of the electron spectra are similar with only some minor differences. The spectra share some characteristics: main peak centers at 0.2 keV μm^{-1}; plateaus are at 0.3 to 0.5 keV μm^{-1}, and 2 to 5 keV μm^{-1}; and a small peak at 10 keV μm^{-1}.

The curves show a lot of fluctuation due to the statistical limitations, which are typical of the microdosimetric problems at the high lineal energy range. In some figures these features show very clearly but they are blurred in other figures. Due to the statistical issues, it is dificult to analyze the differences for the high lineal energy range. One significant difference that can be seen in the figures is that the spectra show a clear peak centered at 0.8 keV μm^{-1} at the entrance part of the phantom, but in parts other than the entrance area the spectra show rather a shoulder in the same lineal energy range. The low energy electrons for which the energy is about 15 keV contributes a lot to the events in the range of 0.4 keV μm^{-1} to 1 keV μm^{-1}. In the secondary particle distribution, the probabilities of particles in the low energy range (below 20 keV) is larger in the area closer to the radiation sources than further away. The distributions show a peak in the range 0.4 keV μm^{-1} to 1 keV μm^{-1} at the x=-300 μm sample area and a shoulder for other areas.

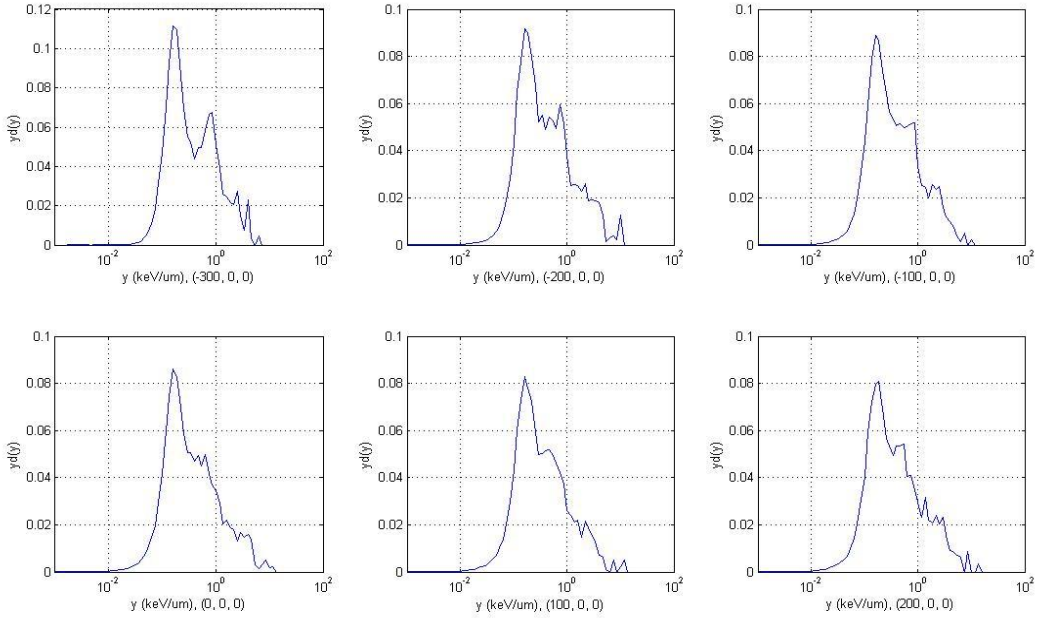

Figure V.8. Microdosimetry spectra of 300 MeV electrons in several sample points along x axis. The coordinates in the figure are in millimeters.

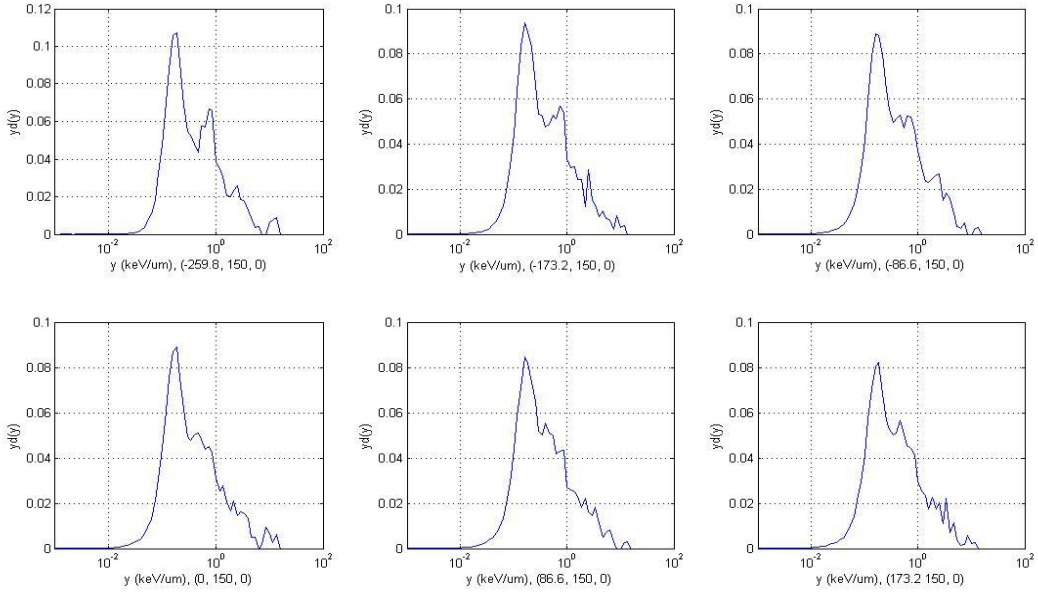

Figure V.9. Microdosimetry spectra of 300 MeV electrons in several sample points along y=150 mm. The coordinates in the figure are in millimeters.

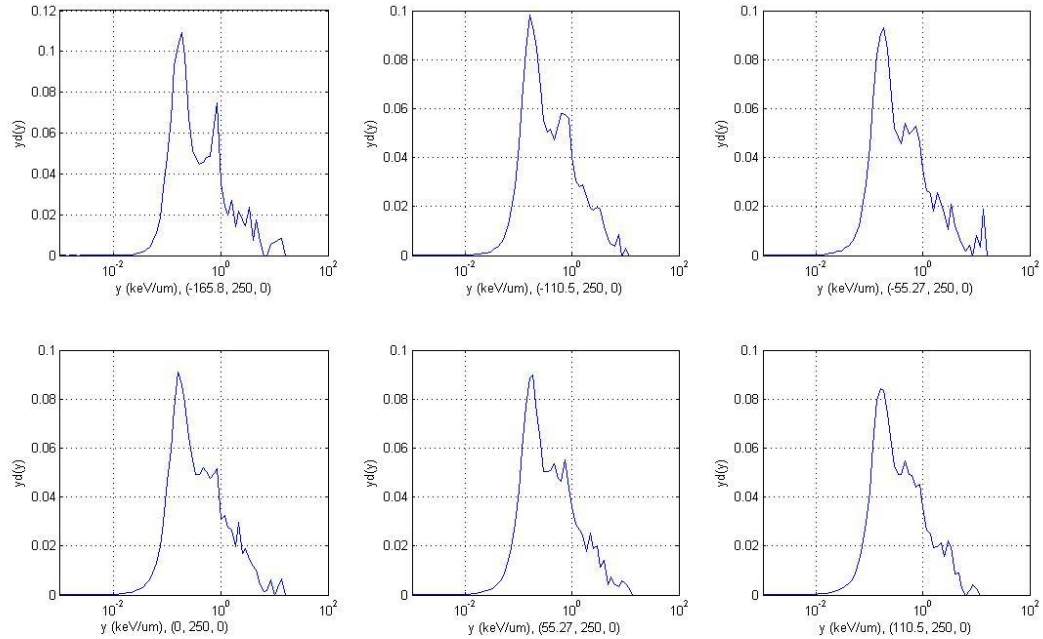

Figure V.10. Microdosimetry spectra of 300 MeV electrons in several sample points along y=250 mm. The coordinates in the figure are in millimeters.

The microdosimetry spectra from different parts of the phantom show no distinct difference in the above figures and the patterns of the curves are almost identical. Although the energy of primary electrons is significantly lower in the extreme right part of the phantom, it does not affect the micordosimetric distribution very much. The secondary electrons distribution is similar in different parts of the phantom (discussed in Section III), and the collision stopping power of the primary particles in the energy range of 80 MeV to 300 MeV is similar with the differences less than 10% (discussed in the introduction Section). So the results are expected to be similar.

To see the details of the curve clearly, the curve from the center sample area of the phantom is shown in Figure V.11. There are two peaks in the curve, one centering at about 0.2 keV μm^{-1} and the other at 10 keV μm^{-1}. And there are shoulders in the curve, ranging from 0.3 keV μm^{-1} to 0.6 keV μm^{-1} and 2 keV μm^{-1} to 5 keV μm^{-1}.

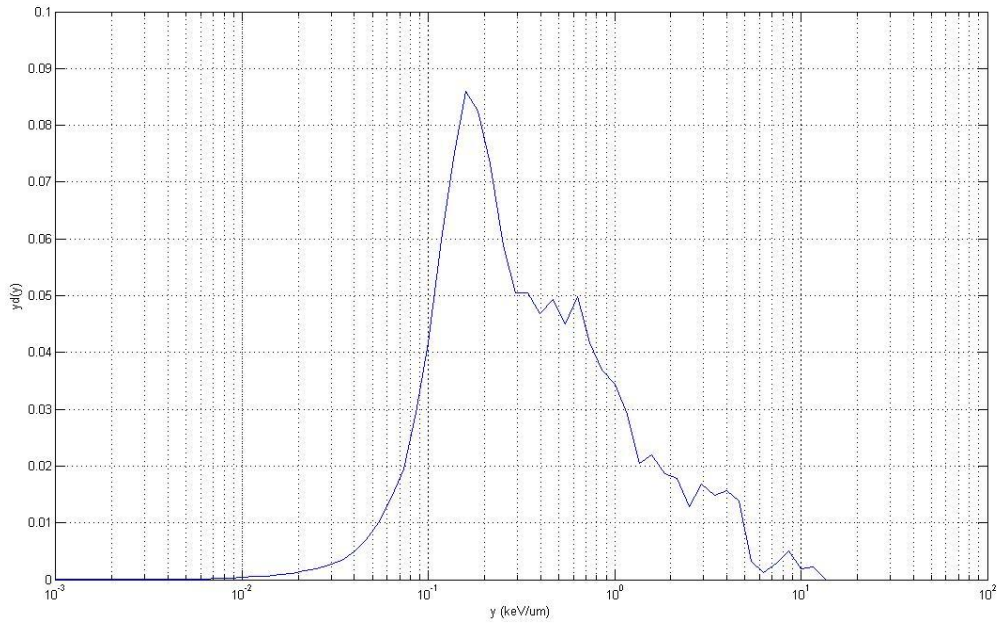

Figure V.11. Microdosimetry spectrum of 300 MeV electrons in the center of the phantom.

V.B.2 Microdosimetry spectra at different cut values

Figure V.12 shows the microdosimetric distributions in different depth of the phantom along X axis with the cut value of 4 μm, which is ½ of the detector diameter. In different depth of the phantoms, the distribution is similar with a main peak centering at 0.2 keV μm^{-1}, and several small peaks or shoulders as the curve is dropping down. The

peaks, positioning at larger than 0.3 keV μm^{-1}, become more and more blurred with the increasing depth. Figure V.13 shows the detailed distribution in the center of the phantom comparing with the spectrum with a cut value of 2 μm. There are apparently no significant differences between the spectra with a cut value of 2 μm and 4 μm in the figure.

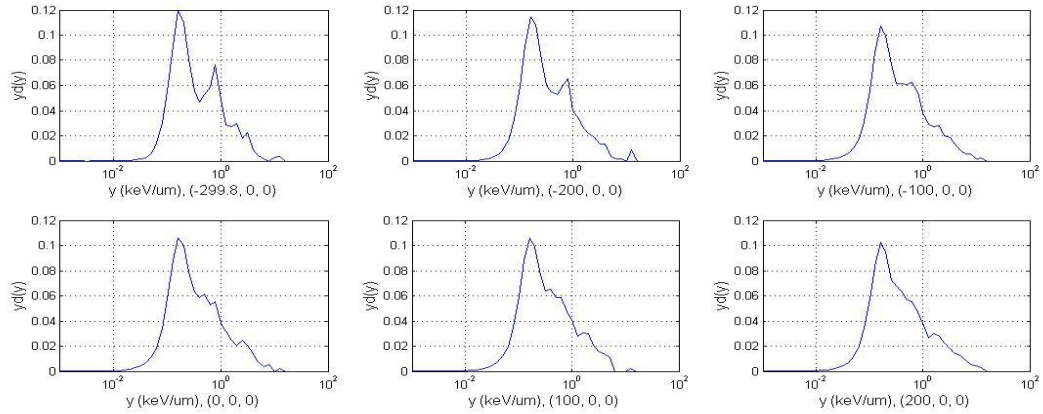

Figure V.12. Microdosimetry spectra of 300 MeV electrons with a cut value of 4 μm. The detector diameter is 8 μm.

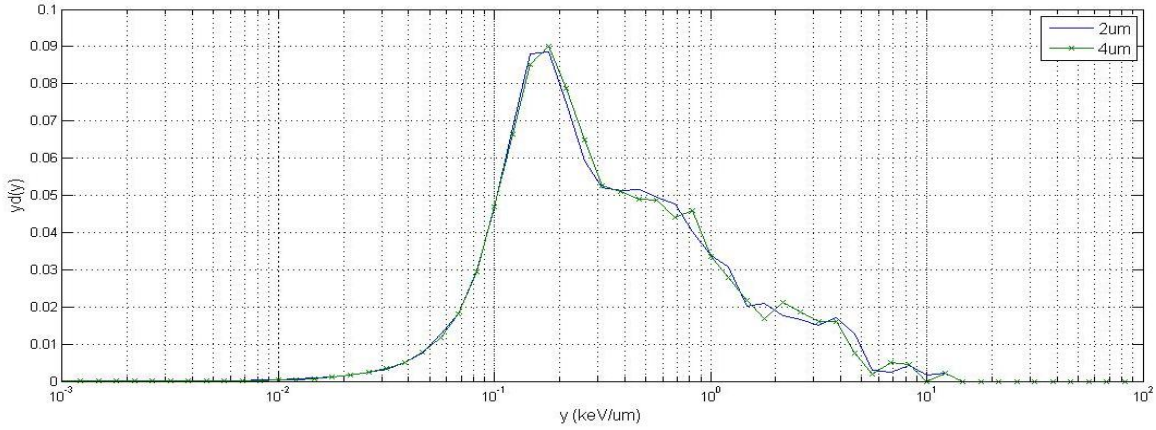

Figure V.13. Microdosimetry spectra of 300 MeV electrons with a cut value of 4 μm and 2 μm in the center of the phantom.

V.B.3 Microdosimetry spectra at different site sizes

The diameter of the detector sites affects the precision of the results but also the simulation time, because with larger diameter the cut value can be set larger. The following two figures (Figure V.14 & V.15) show the microdosimetric distribution at the diameter of 20 μm (simulating with the cut value of 2 μm). The distributions at different depth of the phantom are similar, with the same patterns and peaks locating in the same lineal energy range. Figure V.15 shows changes of microdosimetric distribution with the depth of the sample area in the phantom. With the increasing depth, the peaks centering at 0.2 keV μm^{-1} and 0.4 keV μm^{-1} become lower. The peak centering at 0.2 keV μm^{-1} is due to the primary particles, so it dominates in the entrance area. Very low energy particles contribute a lot to the peak centering at 0.4 keV μm^{-1}. Figure 16 shows the secondary electron energy distribution in two different depths in the phantom, which is plotted in the E^2 f(E) representation. It indicates that the fraction of low energy secondary electrons is larger in the entrance part than that in the deeper area. So height of the peak centered at 0.4 keV μm^{-1} becomes lower with increasing depth.

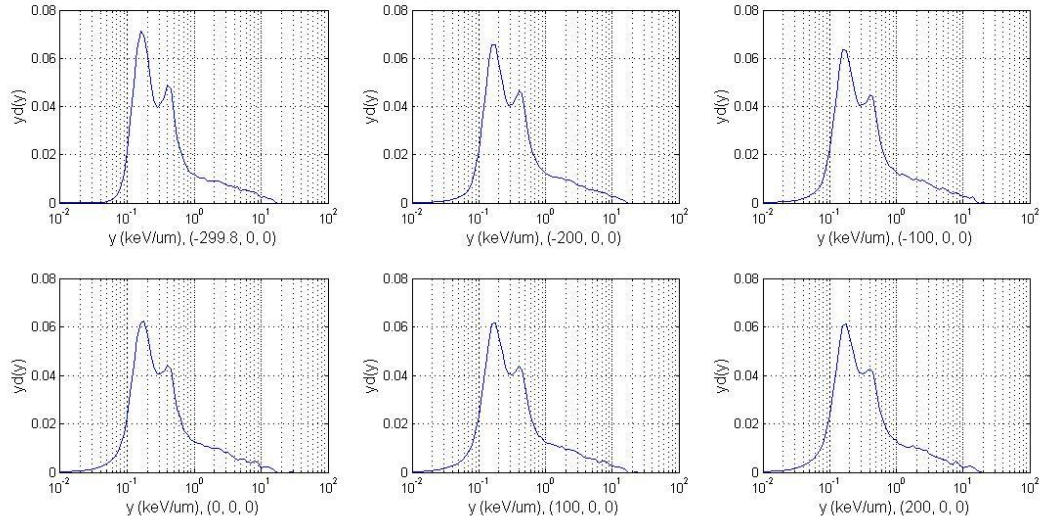

Figure V.14. Microdosimetry spectra of 300 MeV electrons with the detector diameter of 20 μm.

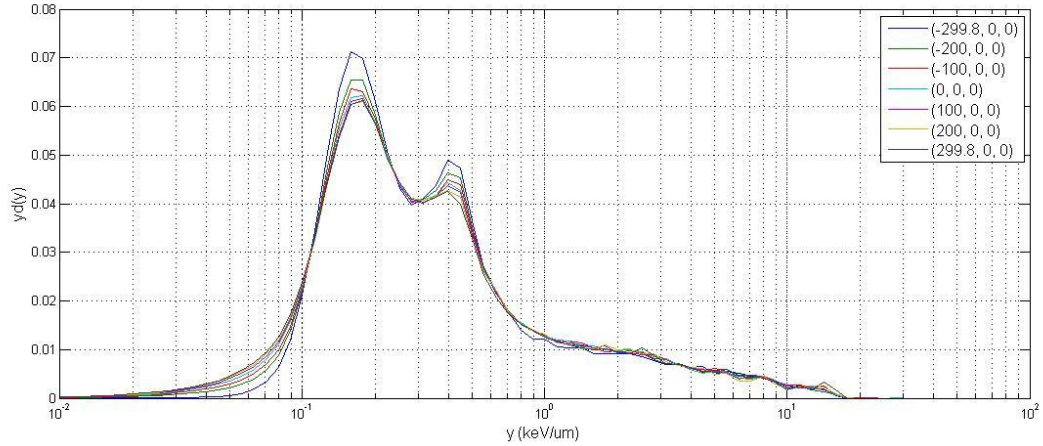

Figure V.15. Differences and similarities of microdosimetric spectra at different depths in the phantom. Detector diameter is 20 μm.

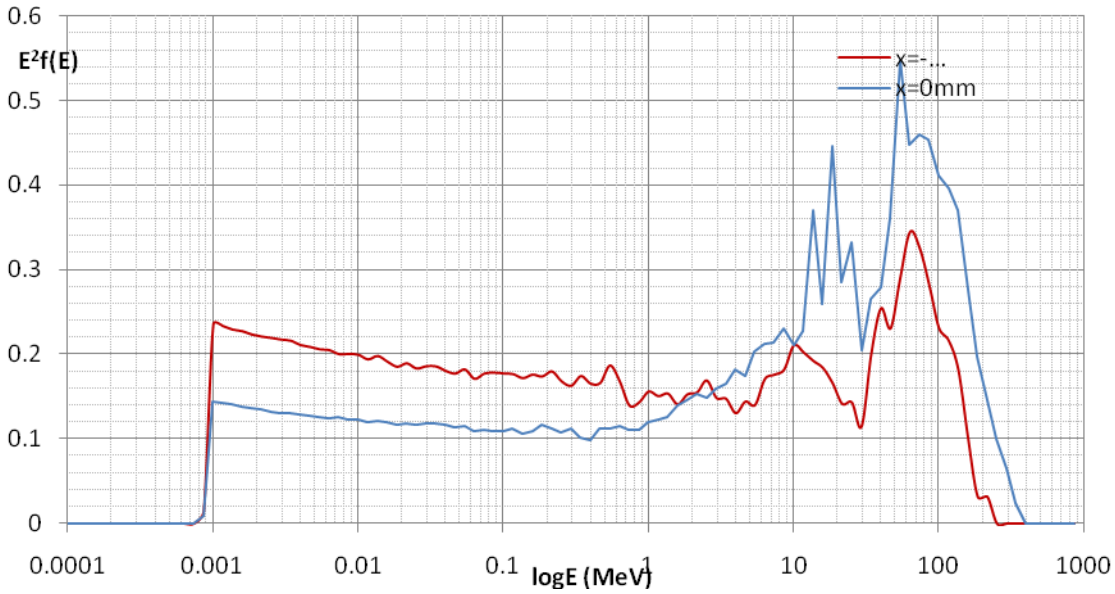

Figure V.16. Secondary electron distributions of 300 MeV in the representation of $E^2f(E)$. The red line is for the distribution in x=-300 mm, where the radiation entrance the phantom. And the blue line is for the distribution in the center of the phantom.

In the range of 1 keV μm^{-1} to 20 keV μm^{-1}, no distinct difference is seen in Figure V.15. But comparing with the results from simulation of a 8 μm diameter site (Figure V.17), some differences are found. In the 8 μm diameter simulation, there are a group of peaks locating between 5 keV μm^{-1} to 20 keV μm^{-1} and a plateau locating from 2 keV μm^{-1} to 4 keV μm^{-1}. In the 20 μm curve, these features are not found clearly, but it seems as the results of smoothing and statistic errors.

The main peak is centering at 0.2 keV μm^{-1} for both curves with similar attitude. The biggest difference between the two curves is the peak locating from 0.3 keV μm^{-1} to 0.6 keV μm^{-1}. The height and the position of the peaks are quite different in the figure. This range of y is dominated by low energy secondary electrons with range less than 8

μm, so the energy imparted may be nearly the same in 8 and 10 μm sites but y is lower in the larger site.

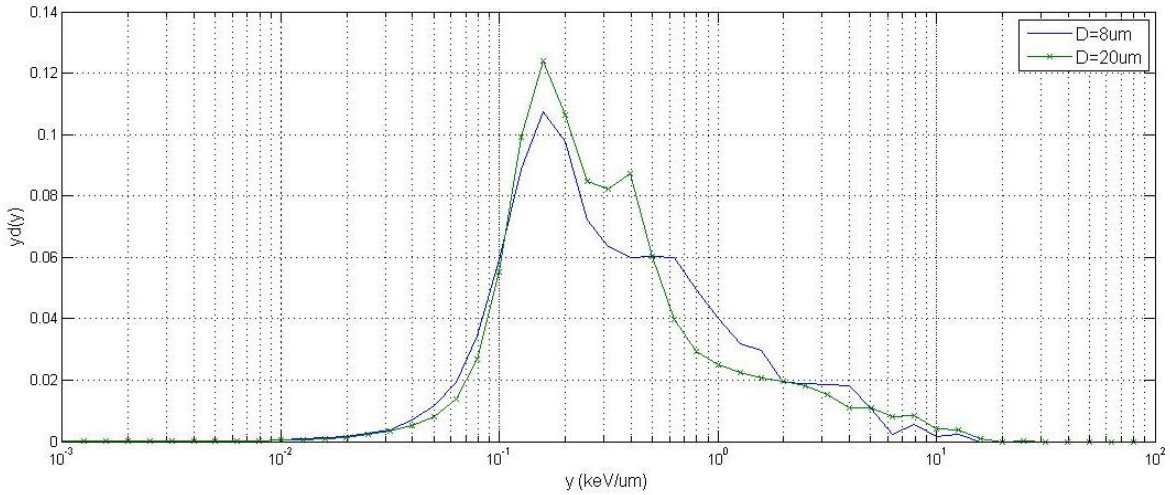

Figure V.17. Comparision of microdosimetric distributions of different site size for electrons.

V.C Cut value and site size effects on the micrososimetric spectra

From the results above, no obvious differences are found between the spectra of electrons or protons. In Geant4 simulation, the software calculates the energy cut values for all kinds of particles that would be used in the simulation, first according to the range cut value. In fact, the mean free path of the particles with the calculated cut energy is much small than the range cut value. So even when the cut value was increased to ½ of the site diameter, no distinct changes were found in the results. In the simulation, 2 μm, ¼ of the site diamter, is small enough for the simulation.

Effects of site size are significant in the spectra for both electron and protons, especially in the y range of 0.4 keV $\mu m^{-1}$to 1 keV μm^{-1}. The larger size of the detector shifts this part of curves left comparing with the smaller size. The effects of site size are

mainly due to the low energy particles. As the cut value was setted as ½ of the diameter, a large amount of low energy particles with ranges smaller than the diamter ware simulated. Thus the y value for the low energy particles is decreased when the site size increased. Comparing the spectra of the electrons and protons, the effects of the site size are almost identical, so either cut value would not change the comparision results of electrons and protons. Considering the biological effects, 8 μm is used for the research.

V.D Experimental data of protons

Figure V.18 shows the microdosimetric spectra of a proton therapy beam measured by a wall-less counter. The spectra are drawn in f(y) and d(y) representations. It is evident from the f(y) spectrum that the majority of the events is due to low energy delta rays. However, the d(y) spectrum shows the delta ray contribution to the absorbed dose to be quite minor.

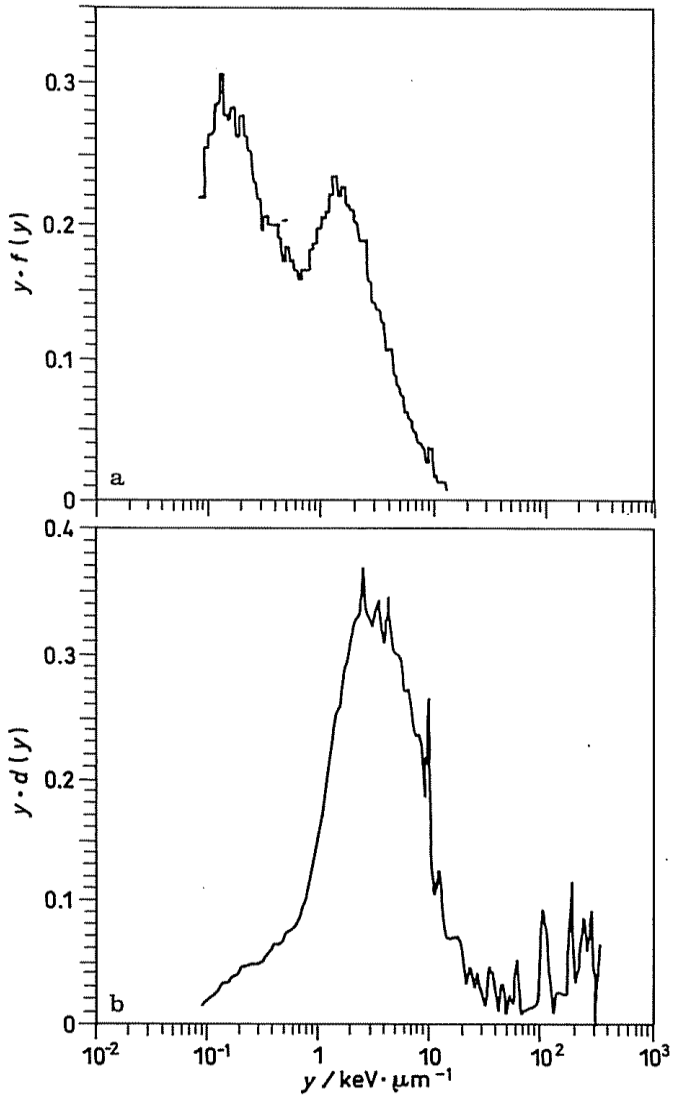

Figure V.18. Microdosimetric spectra for 160 MeV protons. a is in f(y) representation, and b is in d(y) representation. The detector simulated 1 μm diameter sites (Kliauga and Dvorak 1978).

Comparing the 1 GeV simulation data and experimental results of the 160 MeV protons, several differences were found. First, the highest y value for the experimental data of 160 MeV protons is around 300 keV μm^{-1}, but for the 1000 MeV protons it is

about 20 keV μm^{-1}. Second, the events in the range of 1 keV μm^{-1} to 10 keV μm^{-1} contribute most to the dose for 160 MeV, but for the 1000 MeV protons the most contribution range is 0.1 keV μm^{-1} to 1 keV μm^{-1}.

The high y value events are due to the recoil nucleons which have very high stopping power due to their low velocity and high Z value. But usually the recoil nucleons do not have very high energy and so have short range. In the simulation with 8 μm as the detector size, to detect 100 keV μm^{-1} events, the energy of recoil nucleons should be about 600 keV. It is a very high energy for recoil nucleons, so no such events were detected in the simulation.

For 160 MeV protons, the delta rays (y ranging from about 0.1 keV μm^{-1} to 1 keV μm^{-1}) contribute a little to the dose distribution of linear energy, and the primary particles (range from 1 keV μm^{-1} to 10 keV μm^{-1}) contribute most to the dose distribution. The stopping power of protons is shown in Figure V.19. The highest stopping power is about 1000 MeVcm^2g^{-1}, which is 100 keV μm^{-1}, when the protons are about 0.1 MeV. Then the stopping power decreases with the inceasing energy. For the experiment, 160 MeV protons are slowed down to the energy range of 0 to 160 MeV, so the stopping power would be about 1 keV μm^{-1} to 100 keV μm^{-1} (10 MeVcm^2g^{-1} to 1000 MeVcm^2g^{-1}). Considering that the proton energy is very small with stopping power more than 10 keV μm^{-1}, the stopping power of the primary protons would be about 1 keV μm^{-1} to 10 keV μm^{-1} and contribute most to the dose. But in the simulation, 1000 MeV protons were used and the energy when protons exited the phantom was about 850 MeV,

meaning the stopping power was about 2 MeVcm^{2}g^{-1}. Thus the linear energy (y) for the primary protons is 0.2 keVμm^{-1}; the same range of delta rays.

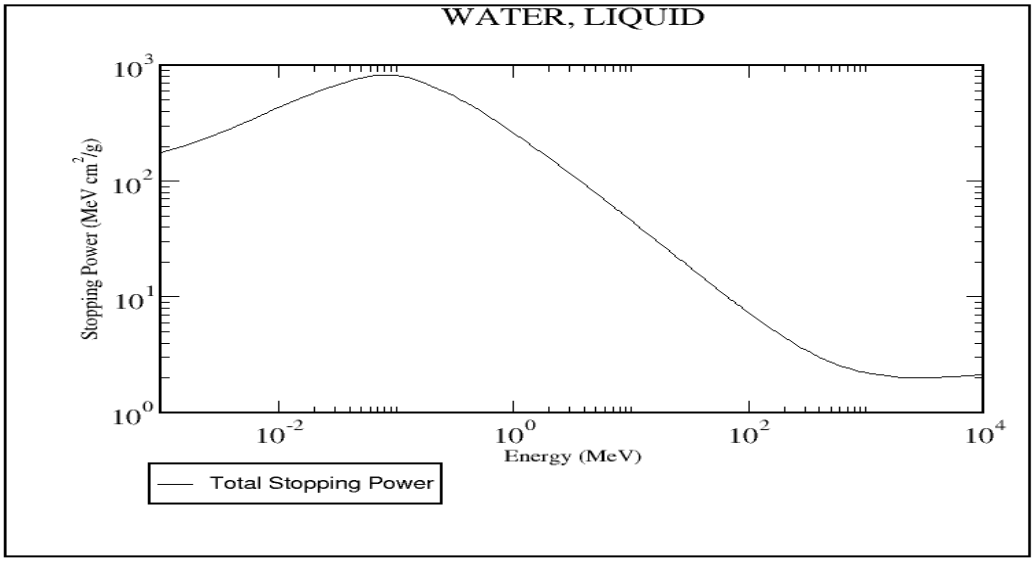

Figure V.19. Proton stopping power in liquid water (Berger et al. 1998).

V.E Comparison of the results of protons and electrons

The following three figures (Figure V.20 to V.22) show the microdosimetric distribution of 1000 MeV protons and 300 MeV electrons in the entrance, center and exiting area of the phantom, respectively. Because the microdosimetric distributions in different position of the phantoms are similar, only spectra from the three samples areas are compared to generate conclusions.

The spectra of 300 MeV electrons are similar to that of 1000 MeV protons: there is a big peak locating around 0.2 keV μm^{-1} in all spectra; a second peak or shoulder is located from 0.4 keV μm^{-1}to 0.9 keV μm^{-1}; and the spectra drop down gradually from 1

to 10 keV μm^{-1} with several shoulders or fluctuations in the range. In addition, there are several small peaks in the y range of 8 keV μm^{-1} to 20 keV μm^{-1} in all of the spectra, but due to the statistic problem the peaks do not locate in the exactly same y range as there are only a few events in one peak. But the important thing is that all the spectra show this feature.

There are also several differences between the spectra of electrons and protons. First, the largest peak of the electrons spectra is located at a little left of the peak for the proton spectra, and the height of the peak is lower especially for the spectra of the exiting area. The biggest difference is in the y range from 0.5 to 0.9 keV μm^{-1}. In the entrance area, the two curves are almost identical in this range, but it is quite different for the spectra in the deeper area. It shows a peak centering at about 0.8 keV μm^{-1} in the protons spectra, but for electrons in the center or the exiting area of the phantom, there is only one shoulder or plateau in the same y range. In other y range, the spectra are similar with minor differences, and the differences are more obviously in the deeper area of the phantoms.

In the figures, it is shown that the curves for the protons are smoother than the spectra for electrons due to the statistic problems. In the simulation of the electrons, fewer primary particles were used to save the simulation time, so less radiation were collected in the sample area.

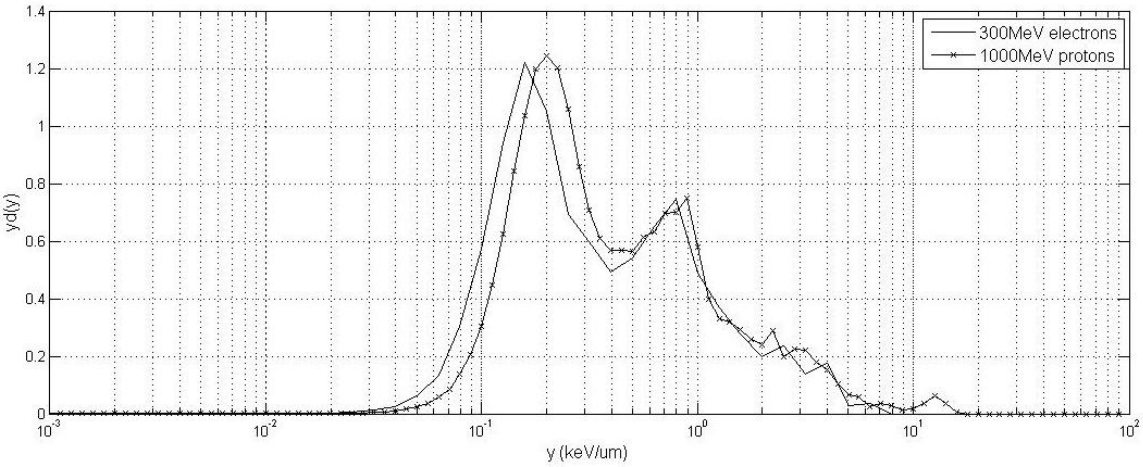

Figure V.20. Microdosimetric dose distributions for protons and electrons in the entrance area of the phantom.

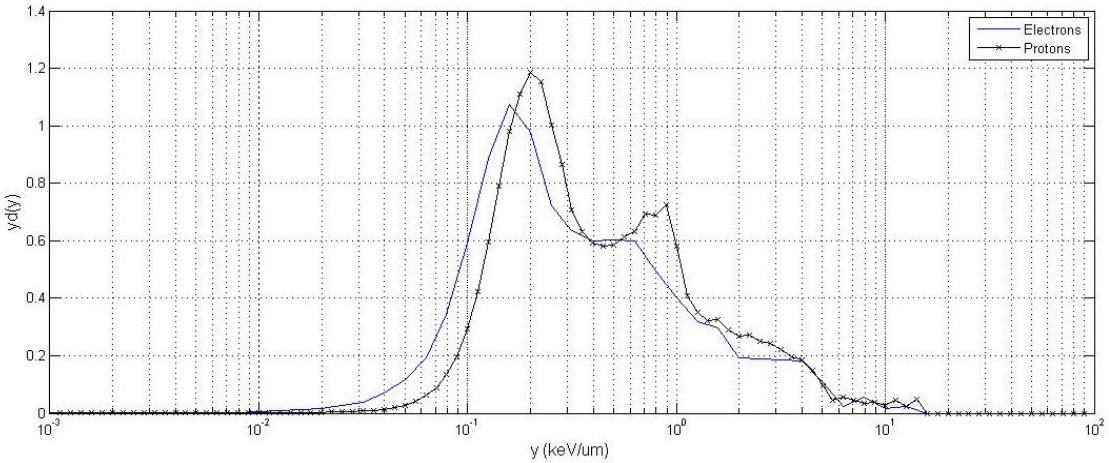

Figure V.21. Microdosimetric dose distributions for protons and electrons in the center of the phantom.

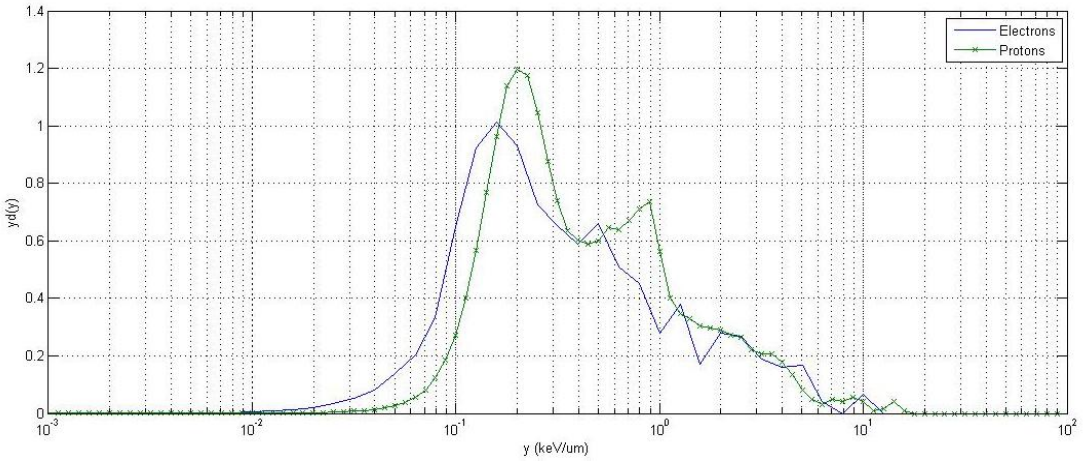

Figure V.22. Microdosimetric dose distributions for protons and electrons in the exiting area of the phantom.

VI. DISCUSSION

Based on the results above, the dose distribution for electrons is much more uniform than the distribution for x rays, but is not uniform as the distribution for protons.. Considering that when doing research on RBE, it is the ratio of the doses of reference radiation to cause particular biological effect to the doses needed for the target radiation, the average dose is used in the calculation of RBE for a phantom. For protons, the average dose along the X axis is about 95% of the maximum value and lowest average dose is 90%of the maximum, so the variance is about 5%. For electrons, the average is 78% of the maximum and the variance is from -25% to +10%. As shown in Figure III.6, in most of the phantom the dose is close to the average. Only a small part, within 40 mm of the edge, the dose is significantly lower (smaller than 95% of the average).

In the experimental research, a layer of tissue equivalent materials could be added between the phantom and the radiation source in contact with the phantom and the electron energy increased to provide the increased range, so the dose in the entrance part of the phantom would be increased. In this way the dose distribution will be more uniform. If this way can increase the dose in the entrance part to 95% of the average dose, and the average dose is the same for protons and electrons. The dose for electrons would be 10% less than the dose of protons in the entrance area, 5% higher in the center, and about the same at 50 mm away from the exiting edge. So the dose distribution of

electron is close enough to that of proton to serve as the reference radiation for research on RBE.

The initial energy distributions of first generation secondary electrons produced by 300 MeV electrons are similar to the distribution of protons at different depths in the phantom, especially in the low energy range. In addition, the collision stopping power of the 300 MeV electrons is similar to the 1000 MeV protons (see Section I). These results indicate that at different depths in the phantom the patterns of the energy deposition would be similar for the reference electrons and the protons.

The spectra of delta rays and microdosimetric dose distributions are similar for 300 MeV electrons and 1000 MeV protons. It indicates that with the same dose the biological effectiveness induced by the 1000 MeV protons is similar to that induced by the 300 MeV electrons. Because the protons are the dominate particles in the cosmic rays, the conclusion could be that the simulation results show that the 300 MeV is a good choice for the reference radiation in the RBE research on cosmic rays. The RBE value for 1000 MeV protons would be approximately one using 300 MeV electrons as the reference radiation. But for cosmic rays, considering high Z-ions and low energy particles which would cause a large portion of high linear energy events, the RBE value would be larger than 1.

Recent studies indicate that the bystander cells (cells that do not experience radiation event) may still contribute to the observed radiation response of a collection cells (Mothersill and Seymour 2001). The bystander effect is a well-established

phenomenon where cells neighboring those directly ‘‘hit’’ by radiation demonstrate a response typical of those actually exposed (Morgan 2003).

The ability partition a population of cells into those that are hit and those that are not is essential for effort to develop mechanism-based models of collective (hit and non-hit) radiation response. Microdosimetry provides a convenient formalism to partition a collection of cells into that are hit and those that are not. (Stewart et al. 2002)

The high energy electrons are available in several departments of energy national laboratories where they are produced by large scale accelerators and thus the electron beams are expensive. For example, the Mainz Microtron in German can generate electrons beams from 180MeV to 855MeV in 15MeV steps (Mainz Microtron 2007).

Laser-plasma accelerators, which have been proposed as the next generation of compact accelerators, would provide high energy electron at a low cost. However it has been difficult to use them efficiently for applications because they have produced poor-quality particle beam with large energy spreads. Recent research found methods to suppress the randomization and the quality of the electron beams can be dramatically enhanced (Faure et al. 2004). In this research, 170 MeV electrons were generated. So it is expected that the high energy electron would be available at a low cost.

In the research of biological effectiveness of radiations, ferrets and mice are often used due the similar syndromes to the human. The CSDA-range of 20 MeV electrons is larger than the size of the animals. The collision stopping power for electrons larger than 1 MeV does not change a lot, so the dose distribution in the animal body would be relative uniform to the proton dose distributions. The secondary particles distribution for

the low energy electrons is similar to the secondary electron distribution of 300 MeV electrons except for the high energy range. It is expected that the microdosimetric dose distribution for the lower energy electrons is similar to the 300 MeV electrons, so in the research on animals, the lower energy electrons can be used as the reference radiation and has similar RBE as the high energy electrons. There are some research works on the low energy electrons for animal experiments (Chao et al. 2009). Currently, the data of the biological effectiveness of several hundreds MeV electrons beams is limited, but there are data on electrons at several tens MeV.

VII. CONCLUSION AND FUTURE WORK

VII.A Conclusion

The dose distribution for protons is more uniform than that of electrons. But by adding a piece of tissue equivalent material in front of the phantom as discussed in part III, the dose distribution of electrons will become much more uniform. Considering the dose distribution, the 300 MeV electrons are appropriate as the reference radiation.

The spectra of delta rays and microdosimetric distributions are similar for 300 MeV electrons and 1000 MeV protons. It indicates that with the same dose the biological effectiveness induced by the 1000 MeV protons is similar to that induced by the 300 MeV electrons. Because the protons are the dominate particles in the cosmic rays, the conclusion could be that the simulation results show that the 300 MeV is a good choice for the reference radiation in the RBE research on cosmic rays.

VII.B Future work

Use other software for microdosimetry. Event-by-event Monte Carlo software, Geant4, is a good choice for its precision, but the low efficient is a significant disadvantage. PENELOPE, for example, is a useful computaionally efficient tool for some classes of microdosimetry probllem. PENELOPE may prove particularly useful for applications that involve radiation transport through materials other than water or for applications that are too computationally intensive for event-by-eventMonte Carlo, such as in vivo microdosimetry of spatially complex distributions of radioisotopes inside the human body (Stewart et al. 2002).

PENELOPE may also prove useful for the estimation of microdosimetric quantities for complex spatial distributions of radioisotopes inside the human body (e.g. radiolabelledmonoclonal antibodies, brachytherapy and other nuclear medicine applications). The estimation of microdosimetric quantities for cell-sized sites is also potentially important for the assessment of health risks associated with the inhalation of metal tritides (Strom et al. 2002) or other inhaled or ingested radioactive materials.

A more detailed model of the human body should be constructed. First, carbon, nitrogen and other elements will be used to more accurately simulate the body material. For basic research, the simple model does not affect the results very significantly. The stopping power in water may be a little different from the human body, and there will be rare carbon or nitrogen atoms backscattering events which result in ions with high stopping power, up to several hundred keV μm^{-1}.

Second, build the skeleton and structures to simulate the organs in the human body. An important part is the bones. In the human body, bone marrow and the bone surface are among the most sensitive organs to radiation. The backscattering near the bone surface will cause the dose distribution to be quite different from other areas for both electrons and protons, which is critical to the bone surface and bone marrow. It is too complicated for the model to include all bones in the body, but in further research simple skeleton of bones would be added to study the affect of bones. Important organs should be also added, so the sensitive organs in the human body could be focused.

REFERENCES

Agostinelli S and Geant4 Collaboration. GEANT4: A simulation toolkit. Nucl. Instrum. Methods Phys. Res. A, 506:250–303; 2003.

Attix FH, Introduction to Radiological Physics and Radiation Dosimetry, Weinheim Germany: WILEY-VCH Verlag GmbH & Co. KGaA; 165-167; 2004.

Berger MJ, Coursey JS, Zucker MA, Chang J. Stopping-power and Range Tables for Electrons, Protons, and Helium Ions [online]. 1998, Updated 2005. Available at: http://www.nist.gov/physlab/data/star/index.cfm. Accessed 1 March 2010.

Chao TC, Chen AM, Tu SJ, Tung CJ, Hong JH, Lee CC. The evaluation of 6 and 18 MeV electron beams for small animal irradiation. Phys. Med. Biol. 54:5847–5860; 2009.

Cucinotta FA, Katz R, Wilson JW, Townsend LW, Nealy JE, Shinn JL. Cellular track model of biological damage to ammalian cell cultures form galactic cosmic rays. NASA Technical Paper 3055; 1991.

Faure J, Glinec Y, Pukhov A, Kiselev S, Gordienko S, Lefebvre E, Rousseau JP, Burgy F, Malka V. A laser-plasma accelerator producing monoenergetic electron beams. Nature 431.7008:541-544; 2004.

Grupen, C, Astroparticle Physics, Heidelberg: Springer; 2005.

ICRU. Radiation Quantities and Units, ICRU Report 33. Bethesda, MD: Int. Comm. Radiat. Units and Meas.; 1980.

International Commission on Radiological Protection (ICRP). Report of the Task Group on Reference Man. Annals of the ICRP 23: 335-362; 1975.

Kliauga PJ, Dvorak R. Microdosimetric measurement of ionization by monoenergetic photons. Radiat. Res 73:1-20; 1978.

Mainz Microtron, Institute for Nuclear Physics of the Johannes Gutenberg University of Mainz. Updated on 4 May 2007. Available at: http://wwwkph.kph.uni-mainz.de/B1//principle.php. Accessed 1 June 2010.

Mishev AL, Mavrodiev SC and Stamenov JN. In Martsch IN eds. Frontiers in Cosmic Rays Research, New York: Nova Science Publishers; 35-83; 2004.

Morgan WF. Non-targeted and delayed effects of exposure to ionizing radiation: II. Radiation-induced genomic instability and bystander effects in vivo, clastogenic factors and transgenerational effects. Radiat. Res. 159:581–596; 2003.

Mothersill C, Seymour C. Radiation-induced bystander effects: past history and future directions. Radiat. Res 155:759–67; 2001.

National Council on Radiation Protection and Measurements (NCRP). The relative biological effectiveness of radiations of different quality. Bethesda, MD; NCRP Publications; NCRP report 104; 1990.

National Space Biomedical Research Institute, Center of Acute Radiation Research. Available at: http://www.nsbri.org/Research/Projects/viewsummary.epl?pid=280. Accessed 1 May 2010.

Rossi HH, Zaider M, Microdosimetry and Its Applications, Heidelberg: Springer; 1996.

Simpson JA, Elemental and isotopic composition of the galactic cosmic rays, Nucl. And Part. Sci., 33:323-382; 1983.

Stewart RD, Wilson WE, McDonald JC, Strom DJ. Microdosimetric properties of ionizing electrons in water: a test of the PENELOPE code system. Phys. Med. Biol. 47:79-88; 2002.

Strom DJ, Stewart RD and McDonald JC. Spectral emissions and dosimetry of metal tritides. Radiat. Prot. Dosim 98:389-400; 2002.

Wroe AJ, Cornelius IM, Rosenfeld AB, Pisacane VL, Ziegler JF, Nelson ME, Cucinotta F, Zaider M, Dicello JF. Microdosimetry simulations of solar protons within a spacecraft. IEEE Transactions on Nuclear Science 52:2591-2596; 2005.

APPENDIX A

GEANT4 TOOLKIT PROGRAM SETTING

In the simulation, range cut value is set to 2 μm. And the energy cut value calculated by Geant4 is 1.25 keV for electrons. In the microdosimetry simulation, about 100 million primary particles were simulated for protons and the beam is a 100 mm square, and the sample points is in the center of the beam line. In the simulatio for dose distribtuion, the dose is about 1 μGy.

To reduce the simulation time, the phantom is devided into several layers, the cut value is different in different layer. The cut valuer is larger in the layer further from the center because the interested area is only a thin layer located at z=0 mm.

VITA

Shaoyong Feng received his Bachelor of Engineering degree in Engineering Physics from Tsinghua University in 2008. He entered the Health Physics program at Texas A&M University in September 2008 and received his Master of Science degree in Augest 2010. His research interests include microdosimetry of high energy particles. Shaoyong Feng may be reached at Department of Nuclear Engineering, Texas A&M University, 3313 TAMU, College Station, TX 77843. His email is feng.shaoyong@gmail.com.